Estimating Spectral Fluxes in Quasi-Two-Dimensional Flows with Advective Structure Functions and Bessel Functions

BRODIE PEARSON,[a] CASSIDY WAGNER,[a] BAYLOR FOX-KEMPER,[b] AND ROGER SAMELSON[a]

[a] College of Earth, Ocean & Atmospheric Sciences, Oregon State University, Corvallis, Oregon
[b] Department of Earth, Environmental & Planetary Sciences, Brown University, Providence, Rhode Island

(Manuscript received 1 November 2024, in final form 30 April 2025, accepted 14 May 2025)

ABSTRACT: Several new methods are proposed that can diagnose the interscale transfer (or spectral flux) of kinetic energy (KE) and other properties in oceanic and broader geophysical systems, using integrals of advective structure functions and Bessel functions (herein "Bessel methods"). The utility of the Bessel methods is evaluated using simulations of anisotropic flow within two-dimensional (2D), surface quasigeostrophic (SQG), and two-layer QG systems. The Bessel methods diagnose various spectral fluxes within all of these systems, even under strong anisotropy and complex dynamics (e.g., multiple cascaded variables, coincident and opposing spectral fluxes, and nonstationary systems). In 2D turbulence, the Bessel methods capture the inverse KE cascade at large scales and the downscale enstrophy cascade (and associated downscale energy flux) at small scales. In SQG turbulence, the Bessel methods capture the downscale buoyancy variance cascade and the coincident upscale wavenumber-dependent KE flux. In QG turbulence, the Bessel methods capture the upscale kinetic energy flux. It is shown that these Bessel methods can be applied to data with limited extent or resolution, provided the scales of interest are captured by the range of separation distances. The Bessel methods are shown to have several advantages over other flux-estimation methods, including the ability to diagnose downscale energy cascades and to identify sharp transition scales. Analogous Bessel methods are also discussed for third-order structure functions, along with some caveats due to boundary terms.

SIGNIFICANCE STATEMENT: Big ocean eddies play an important role in Earth's energy cycle by moving energy to both larger and smaller scales, but it is difficult to measure these "eddy energy fluxes" from oceanic observations. We develop a new method to estimate eddy energy fluxes that utilizes spatial differences between pairs of points and can be applied to various ocean data. This new method accurately diagnoses key eddy energy flux properties, as we demonstrate using idealized numerical simulations of various large-scale ocean systems.

KEYWORDS: Ocean; Eddies; Energy transport; Mesoscale processes; Turbulence

1. Introduction

Various processes supply energy to the ocean and much of this energy passes through mesoscale (10–500 km) eddies, which are quasi-two-dimensional (quasi-2D) turbulent motions ubiquitous across the global ocean (Chelton et al. 2011). The energy cycle, which describes how energy moves between scales (via spectral fluxes) or locations (via spatial fluxes), and the resultant fate of the ocean's energy have implications for the large-scale circulation and Earth's broader climate (Klein et al. 2019; Hewitt et al. 2022). Recent and future technological advances will enable us to explore ocean mesoscale dynamics and the energy cycle at an unprecedented scale through in situ measurements (Johnson et al. 2022), remote sensing (Morrow et al. 2023), and mesoscale-resolving numerical models (Silvestri et al. 2025). However, it is generally not possible to directly measure mesoscale spectral fluxes of energy fluxes from observations. Theoretically, quasi-2D turbulence is characterized by an inverse cascade of kinetic energy to larger scales (Boffetta and Ecke 2012), but recent observations suggest that mesoscale turbulence could move energy to both larger and smaller scales (Balwada et al. 2022).

The primary goal of this manuscript's work is to better estimate 2D spectral fluxes of energy Π_K^u at different scales, in addition to the fluxes of other scalar halved variances Π_K^ϕ:

$$\Pi_K^u = -\oint\!\!\oint_{\kappa \geq K} \mathrm{Re}[\widehat{\mathbf{u}}^* \cdot \widehat{\mathbf{u} \cdot \nabla \mathbf{u}}]\,dk\,dl,$$
$$\Pi_K^\phi = -\oint\!\!\oint_{\kappa \geq K} \mathrm{Re}[\widehat{\phi}^* \widehat{\mathbf{u} \cdot \nabla \phi}]\,dk\,dl. \quad (1)$$

Here, $\mathbf{k} = (k, l)$ is the 2D wavenumber vector; $\kappa = \sqrt{k^2 + l^2}$ is the wavenumber magnitude; $\mathbf{u}$ is the 2D velocity vector; ϕ is a generic scalar field; the hat and * symbols denote a Fourier transform and complex conjugate, respectively; and K is the wavenumber (scale) at which the calculated flux is occurring. The challenges of calculating the above flux and associated Fourier transforms from realistic or complex datasets, due to irregular or nonperiodic data, have led to the development of other statistical tools to estimate these fluxes from oceanographic and geophysical data. These methods include coarse graining (Aluie et al. 2018), temporal spectral analysis (Arbic et al. 2012), and structure functions (Kolmogorov 1941; Lindborg 1999). Here, we will focus on structure functions, which are constructed from averaged spatial differences in flow properties. Several useful velocity ($\mathbf{u}$)-based structure functions include

Corresponding author: Brodie Pearson, brodie.pearson@oregonstate.edu

DOI: 10.1175/JPO-D-24-0211.1

$$\mathrm{SF}_{LLL} = \overline{\delta u_L \delta u_L \delta u_L}, \tag{2}$$

$$\mathrm{SF}_{Luu} = \overline{\delta u_L (\delta \mathbf{u} \cdot \delta \mathbf{u})}, \tag{3}$$

$$\mathrm{SF}_{uuu} = \overline{\delta \mathbf{u} (\delta \mathbf{u} \cdot \delta \mathbf{u})}, \tag{4}$$

$$\mathrm{SF}_{\mathcal{A}u} = \overline{\delta \mathbf{u} \cdot \delta \mathcal{A}_u}, \text{ where } \mathcal{A}_u = (\mathbf{u} \cdot \nabla)\mathbf{u}. \tag{5}$$

Here, $\delta\phi = [\phi(\mathbf{x} + \mathbf{r}) - \phi(\mathbf{x})]$ represents the spatial difference in ϕ, $\mathbf{r}$ represents the separation vector, $u_L = \mathbf{u} \cdot \hat{\mathbf{r}}$ is the longitudinal velocity component with $\hat{\mathbf{r}} = \mathbf{r}/|\mathbf{r}|$, and the overline represents an average over positions $\mathbf{x}$, time, and/or ensemble. The first three relations [Eqs. (2)–(4)] define several types of third-order velocity structure functions that have been used to study turbulent flows (Lindborg 1999; Deusebio et al. 2014; Pearson et al. 2020; Balwada et al. 2022). The final relation [Eq. (5)] defines the advective velocity structure function $\mathrm{SF}_{\mathcal{A}u}$ introduced by Pearson et al. (2021). In contrast to the other structure functions above, $\mathrm{SF}_{\mathcal{A}u}$ is a second-order structure function (SF) (it only contains two δ terms) and it contains a local derivative of the flow field. As a result, $\mathrm{SF}_{\mathcal{A}u}$ provides statistical benefits and poses diagnostic challenges compared to the other SFs (Pearson et al. 2021).

Estimates of Π_K^u from third-order velocity structure functions typically use "inertial-range (IR) methods" which assume the generic form:

$$\Pi_K^u \approx \frac{\mathrm{SF} r^{-n}}{a}, \tag{6}$$

where a and n are constants that depend on the specific structure function being utilized. For example, $\Pi_K^u \approx \mathrm{SF}_{uuL} r^{-1}/2$ or $\Pi_K^u \approx \mathrm{SF}_{LLL} r^{-1}/(3/2)$ (Lindborg 1999). This form can be inferred from the properties of the Navier–Stokes equations, but its derivation requires assumptions including, as IR terminology suggests, the presence of an inertial cascade (i.e., Π_K is the constant across a wide-enough range of scales around $r = |\mathbf{r}|$) and isotropy of the turbulent flow. The IR method fails to estimate Π_K^u accurately when turbulence is anisotropic (Pearson et al. 2021).

The advective velocity structure function $\mathrm{SF}_{\mathcal{A}u}$ can also be used to estimate Π_K^u in 2D turbulence through the IR method ($\Pi_K^u \approx \mathrm{SF}_{\mathcal{A}u}/2$), even when the flow is highly anisotropic (Pearson et al. 2021). Pearson et al. (2021) demonstrated several statistical and practical advantages of advective structure functions, over their third-order counterparts, for estimating the upscale flux of kinetic energy Π_K^u and the downscale flux of enstrophy Π_K^ω in anisotropic 2D turbulence, using the IR method. However, these advective structure function methods are still not able to quantify several important aspects of quasi-2D flows as we will demonstrate.

Xie and Bühler (2018) proposed an alternative method to relate Π_K^u and third-order structure functions through the integration of structure functions and Bessel functions. This method has been used to infer information about Π_K^u from ocean drifter data (Balwada et al. 2022) and within simulated 2D magnetohydrodynamical turbulence with upscale and downscale energy transfer (Xie and Bühler 2019). In this study, we present a new "Bessel method" for diagnosing spectral fluxes in quasi-2D turbulence through integration of advective structure functions and Bessel functions. We demonstrate the utility of this Bessel method for several anisotropic quasi-2D systems relevant to large-scale ocean dynamics, spanning 2D, surface quasigeostrophic (SQG), and multilayer QG turbulence, and contrast against other common flux-estimation methods.

2. Methods

a. Geophysical (quasi-2D) turbulence

In this study, numerical simulations of three distinct quasi-2D systems are used to explore a new method for diagnosing various spectral fluxes in geophysical turbulence. These systems are 2D turbulence, SQG turbulence, and two-layer QG turbulence. In all of these systems, there is an incompressible velocity field $\mathbf{u} = (u, v) = (-\partial_y\psi, \partial_x\psi)$ described by a streamfunction ψ, and the evolution of the system is described through a prognostic equation for a single, dynamically important scalar that is also a function of the streamfunction (in the QG case, there is one scalar for each layer). All these systems also include a β effect to create anisotropic dynamics, forcing F to supply energy, and damping D to remove energy. Here, we summarize the governing dynamics of the three systems to set up the new methods. The details of the simulation parameters are described in section 2f:

The 2D system is simulated by evolving vorticity $\omega = \nabla^2\psi = \hat{\mathbf{z}} \cdot (\nabla \times \mathbf{u})$,

$$\frac{\partial \omega}{\partial t} + \mathbf{u} \cdot \nabla\omega + v\beta_{2\mathrm{d}} = D_{2\mathrm{d}} + F_{2\mathrm{d}}. \tag{7}$$

In this system, an "inverse" cascade of energy to larger scales and a "downscale" cascade of enstrophy ($\eta = \omega^2/2$) to smaller scales are expected (Kraichnan 1967; Boffetta and Ecke 2012).

The SQG system is simulated by evolving a surface buoyancy field $b = -\partial_z\psi$ under the assumption of zero interior potential vorticity ($q = \omega + \partial_z^2\psi = 0$):

$$\frac{\partial b}{\partial t} + \mathbf{u} \cdot \nabla b + v\beta_{\mathrm{sqg}} = D_{\mathrm{sqg}} + F_{\mathrm{sqg}}. \tag{8}$$

In this system, we expect a downscale cascade of buoyancy variance to smaller scales, alongside an upscale flux of energy that increases at larger scales (Capet et al. 2008).

The two-layer QG system is simulated by evolving the potential vorticity of each layer (Salmon 1980; Smith and Vallis 2002):

$$\frac{\partial q_i}{\partial t} + \mathbf{u}_i \cdot \nabla q_i + v_i\beta_{\mathrm{qg}} = D_{\mathrm{qg},i} + F_{\mathrm{qg},i}. \tag{9}$$

Here, the potential vorticity of the top ($i = 1$) and bottom ($i = 2$) layers is given by $q_{1,2} = \omega_{1,2} + \Gamma_{1,2}(\psi_{2,1} - \psi_{1,2})$, where Γ_i is described in section 2f. In this system, the total energy is conserved (Vallis 2006), but this energy can be transferred between kinetic energy and potential energy through variations

in the layer interface height. In the following analyses, we will explore spectral fluxes of dynamical quantities: kinetic energy, potential enstrophy ($q^2/2$), and enstrophy ($\omega^2/2$).

The momentum and the above evolved variables are related through the streamfunction, with distinct relations for the 2D, SQG, and QG systems. However, in all these systems, the momentum budget takes the form:

$$\frac{\partial \mathbf{u}}{\partial t} + (\mathbf{u}\cdot\nabla)\mathbf{u} = \text{other physics}, \tag{10}$$

where momentum is advected in space, and there are additional physics that vary between systems (e.g., Vallis 2006; Capet et al. 2008; Boffetta and Ecke 2012). The presence of the advective term in Eq. (10) [and Eqs. (7)–(9)] enables the use of advective structure functions to diagnose spectral fluxes of kinetic energy (and scalar variances) in all of these systems, as we discuss in the next section.

b. *Diagnosing spectral fluxes from structure functions*

SPECTRAL FLUXES OF KINETIC ENERGY

The budget for the two-dimensional kinetic energy spectrum ($E_K = \widehat{|\mathbf{u}|}^2/2$) at a particular wavenumber $|\mathbf{k}| = K$ follows from the momentum budget [Eq. (10)] for the 2D, SQG, and QG systems as

$$\frac{\partial E_K}{\partial t} = \frac{1}{2}\widehat{\mathbf{u}}^*\cdot\widehat{\frac{\partial \mathbf{u}}{\partial t}} + \frac{1}{2}\widehat{\mathbf{u}}\cdot\widehat{\frac{\partial \mathbf{u}}{\partial t}}^* = \underbrace{-\mathrm{Re}\{\widehat{\mathbf{u}}^*\cdot\widehat{(\mathbf{u}\cdot\nabla)\mathbf{u}}\}}_{T_K} + \text{other physics}, \tag{11}$$

where the other physics details do not matter for the following derivations but can include sinks of energy (dissipation), sources of energy (forcing), and transfers between energy reservoirs (in the SQG and QG systems).

The first term on the right-hand side of Eq. (11) is often called the transfer function T_K, and it describes how energy is moved between wavenumbers by nonlinear dynamics. It can be related to the spectral flux of energy via $\Pi^u_K = \iint_{\kappa\geq K} T_\kappa d\kappa dl = -\iint_{\kappa<K} T_\kappa d\kappa dl$ (Boffetta and Ecke 2012; Pearson et al. 2021; Zhang et al. 2024). The transfer function is also related to structure functions via the Karman–Howarth–Monin (KHM) equation which allows us to express

$$T_K = \frac{1}{2}\widehat{\mathrm{SF}_{\mathcal{A}u}} = \frac{1}{4}\nabla\cdot\widehat{\mathrm{SF}_{uuu}}, \tag{12}$$

where the first equivalence mirrors the advective term that provides the source of T_K, while the second equivalence follows under incompressible conditions (Frisch 1995).

The above transfer function relations allow the spectral flux to be expressed via an integral of the advective structure function over the smallest wavenumbers ($\kappa < K$) or equivalently an integral over all wavenumbers of the product between the advective structure function and the Heaviside function H:

$$\Pi^u_K = -\frac{1}{2}\iint \widehat{\mathrm{SF}_{\mathcal{A}u}} H(K-\kappa) d\kappa dl. \tag{13}$$

Using the Plancherel theorem, this can be converted to an expression relating the energy flux to a real-space integral involving the advective structure function and a Bessel function of the first kind (see appendix A for derivation):

$$\Pi^u_K = -\frac{K}{4\pi}\int_0^\infty \left[\int_0^{2\pi} \mathrm{SF}_{\mathcal{A}u}(\mathbf{r}) d\theta\right] J_1(Kr) dr = -\frac{K}{2}\int_0^\infty \widetilde{\mathrm{SF}}_{\mathcal{A}u} J_1(Kr) dr, \tag{14}$$

where J_n represents the nth Bessel function of the first kind, and we introduce a short-hand notation for the angle-averaged advective structure function at each separation distance $\left[\widetilde{\mathrm{SF}}_{\mathcal{A}u} = \widetilde{\mathrm{SF}}_{\mathcal{A}u}(r) = \int_0^{2\pi} \mathrm{SF}_{\mathcal{A}u}(\mathbf{r}) d\theta/2\pi\right]$. Importantly, in deriving Eq. (14), there is no need to assume isotropy of the flow or its statistics [e.g., we did not assume $\mathrm{SF}_{\mathcal{A}u}(\mathbf{r}) = \widetilde{\mathrm{SF}}_{\mathcal{A}u}(r)$ for all separation directions]. Similar angle-averaged third-order structure functions have been considered previously (e.g., Lindborg 1996; Nie and Tanveer 1999). Pearson et al. (2021) demonstrated that advective structure functions show less angular variation than third-order structure functions in anisotropic 2D turbulence, suggesting that data from a single (or limited) direction may still be useful for this method.

This angular invariance of the advective structure functions was attributed to its flux-estimate derivation not requiring an assumption of isotropy, in contrast to analogous third-order relations. Another source of statistical isotropy could be compensation between the variations of velocity gradients within $\mathrm{SF}_{\mathcal{A}u}$, which was shown to reduce the temporal intermittency of $\mathrm{SF}_{\mathcal{A}u}$ in 2D turbulence (Pearson et al. 2021). Although turbulent velocity gradients display intermittency, the different gradients and their fluctuations are coupled through incompressibility and vorticity constraints in 2D turbulence (Pearson et al. 2021). The isotropy of $\mathrm{SF}_{\mathcal{A}u}$ could be system dependent and may change, for example, if there is 2D compressibility (SQG) or potential vorticity dynamics (two-layer QG).

As we will show in the present paper, this new relation can be used to diagnose the spectral flux Π^u_K from measurements of the advective structure function, even when fluid flow is anisotropic and Π^u_K varies with K. Equation (14) for the advective velocity structure function is analogous to two relations presented by Xie and Bühler (2018) for the third-order velocity structure functions SF_{Luu} and SF_{LLL} in 2D turbulence under the assumption of isotropic flow statistics and incompressibility:

$$\Pi^u_K = -\frac{K^2}{4}\int_0^\infty \widetilde{\mathrm{SF}}_{Luu} J_2(Kr) dr - \xi_{uuL}, \tag{15}$$

$$= -\frac{K^3}{12}\int_0^\infty \widetilde{\mathrm{SF}}_{LLL} J_3(Kr) r dr - \xi_{uuL} - \xi_{LLL}, \tag{16}$$

where ξ terms represent the functions that arise from integration by parts (see appendix B for details). The Xie and Bühler (2018) relations neglect the ξ terms in Eqs. (15) and (16), although these terms typically do not vanish and can result in noisy estimates of Π^u_K, even in idealized simulations (appendix B). Relations for SF_{Luu} analogous to Eq. (15) have been used to estimate energy

flux rates within the upper ocean using drifter observations (Balwada et al. 2022).

c. Spectral fluxes of enstrophy

In 2D turbulence, there is also a downscale cascade of enstrophy $\eta = (1/2)\omega^2$. Following Eq. (7), an equation for the enstrophy power spectrum can be derived that is analogous to Eq. (11). Similarly, the spectral flux of enstrophy Π^{ω}_{K} can be expressed in terms of the advective vorticity structure function $\mathrm{SF}_{\mathcal{A}\omega} = \overline{\delta\omega\delta\mathcal{A}_{\omega}}$ (where $\mathcal{A}_{\omega} = \mathbf{u}\cdot\nabla\omega$):

$$\Pi^{\omega}_{K} = -\frac{K}{2}\int_0^{\infty} \widetilde{\mathrm{SF}}_{\mathcal{A}\omega} J_1(Kr)dr. \tag{17}$$

Integrating by parts and using relations between structure functions $\mathrm{SF}_{\mathcal{A}\omega} = \nabla\cdot\mathrm{SF}_{uu\omega\omega} = -\nabla^2\mathrm{SF}_{\mathcal{A}u}$ (where both relations require horizontal incompressibility), we also find

$$\Pi^{\omega}_{K} = \frac{K^3}{2}\int_0^{\infty} \widetilde{\mathrm{SF}}_{\mathcal{A}u}\left[J_3(Kr) - \frac{2}{Kr}J_2(Kr)\right]dr + \xi^{\omega}_{\mathcal{A}u}, \tag{18}$$

$$= -\frac{K^2}{4}\int_0^{\infty} \widetilde{\mathrm{SF}}_{\omega\omega L} J_2(Kr)dr - \xi^{\omega}_{\omega\omega L}, \tag{19}$$

where the ξ^{ω} terms are analogous to the ξ terms introduced in Eqs. (15) and (16).

d. Spectral fluxes in quasigeostrophic systems

In quasigeostrophic flows, kinetic energy cycles are still important, but other important cascades can also develop. Generally, we can construct relations between spectral fluxes and advective structure functions for any advected flow property, but we will focus on the governing variables in each system, surface buoyancy [SQG; Eq. (8)], and potential vorticity [QG; Eq. (9)]. These relations are direct analogies to the energy and enstrophy relations [Eqs. (14) and (17)], but we shall state them below for clarity.

In SQG turbulence, surface buoyancy variance (divided by two, for consistency with energy and enstrophy) is cascaded to small scales by a spectral flux (Π^{b}_{K}) which can be diagnosed by

$$\Pi^{b}_{K} = -\frac{K}{2}\int_0^{\infty} \widetilde{\mathrm{SF}}_{\mathcal{A}b} J_1(Kr)dr. \tag{20}$$

In QG turbulence, there is a downscale cascade of potential enstrophy ($q^2/2$; where q is the potential vorticity). The spectral flux of potential enstrophy can be estimated as

$$\Pi^{q}_{K} = -\frac{K}{2}\int_0^{\infty} \widetilde{\mathrm{SF}}_{\mathcal{A}q} J_1(\mathrm{Kr})dr. \tag{21}$$

It is common to only measure dynamical information at the ocean surface, in which case q cannot be diagnosed since it depends on the streamfunction in multiple layers. In this case, it is still useful to explore the vorticity (ω), and the associated spectral flux of enstrophy (Π^{ω}_{K}) which could be estimated through Eqs. (17) and (18), analogous to 2D turbulence. Note that it is also common to use the terms enstrophy $[(1/2)q^2]$ and relative enstrophy $[(1/2)\omega^2]$ in QG turbulence (e.g., Vallis 2006), but here we use the terms potential enstrophy $[(1/2)q^2]$ and enstrophy $[(1/2)\omega^2]$ to draw parallels with 2D turbulence and to avoid confusion.

e. Implications for IR methods of structure function analysis

Traditionally, structure functions (defined in r space) have been used to estimate spectral fluxes (defined in K space) through IR methods that use proportionality relations. The Bessel method relations between structure functions and spectral fluxes derived above can provide some insight into the appropriate remapping from r space to K space for the structure function proportionality methods. Note that the following discussion does not present an exact or direct remapping, since the Bessel method relies on integrals of products, but is intended to provide insight into the appropriate ways to contrast and interpret information from IR methods using different structure functions.

The new Bessel methods in Eqs. (14)–(21) involve integrals of the product of structure functions and Bessel functions. These Bessel functions are oscillatory and decay (Fig. A1), so the integrals at a given wavenumber K provide the greatest weight to the structure function located at the first peak of the Bessel function ($r_{\mathrm{peak}} = z_{\mathrm{peak}}/K$). The location of this maximum value moves to larger z (or Kr) for higher-order Bessel functions, which indicates that the factor used in $r \to K$ remapping should depend on the structure function being used and the flux being diagnosed, since these affect the convolved Bessel function. Specifically, the maxima of $J_1(z)$, $J_2(z)$, and $J_3(z)$ occur at approximately $z_{\mathrm{peak}} = Kr_{\mathrm{peak}} \approx 2$, 3.1, and 4.3, respectively (Fig. A1). This suggests that IR method relations utilizing J_1 should map as $\mathrm{SF}(r) \to \mathrm{Flux}(K \approx 2/r)$ (energy flux from $\mathrm{SF}_{\mathcal{A}u}$; enstrophy flux from $\mathrm{SF}_{\mathcal{A}\omega}$; etc.). Similarly, relations using J_2 should map as $\mathrm{SF}(r) \to \mathrm{Flux}(K \approx 3.1/r)$ (energy flux from SF_{uuL}; enstrophy flux from $\mathrm{SF}_{\omega\omega L}$; etc.), and relations using $rJ_3(r)$ should map as $\mathrm{SF}(r) \to \mathrm{Flux}(K \approx 4.6/r)$ (energy flux from SF_{LLL}). Similar relations can be derived for more general functions, such as that in Eq. (18) which results in $\mathrm{SF}(r) \to \mathrm{Flux}(K \approx 1.5/r)$. Analogous mapping relations have been discussed previously, for example, in section 6 of Davidson (2004).

It is also interesting to note the contrast between Bessel functions, which decay as $(Kr)^{-1/2}$ as $Kr \to \infty$ (Abramowitz and Stegun 1948), and cosine transforms, which are global (they do not decay for large values). This distinction suggests that structure–function relations for two-dimensional datasets [which utilize Bessel functions; Eqs. (14)–(21)] are relatively local compared to the cosine-transform-based relations that arise for one-dimensional datasets [e.g., Webb (1964) or appendix A of McCaffrey et al. (2015)].

f. Simulation details

All the following simulations were conducted with GeophysicalFlows (Constantinou et al. 2021), a Julia-based package for simulating various idealized geophysical systems via pseudo-spectral methods. All simulations were conducted in periodic square domains of width 2π (all variables are nondimensional),

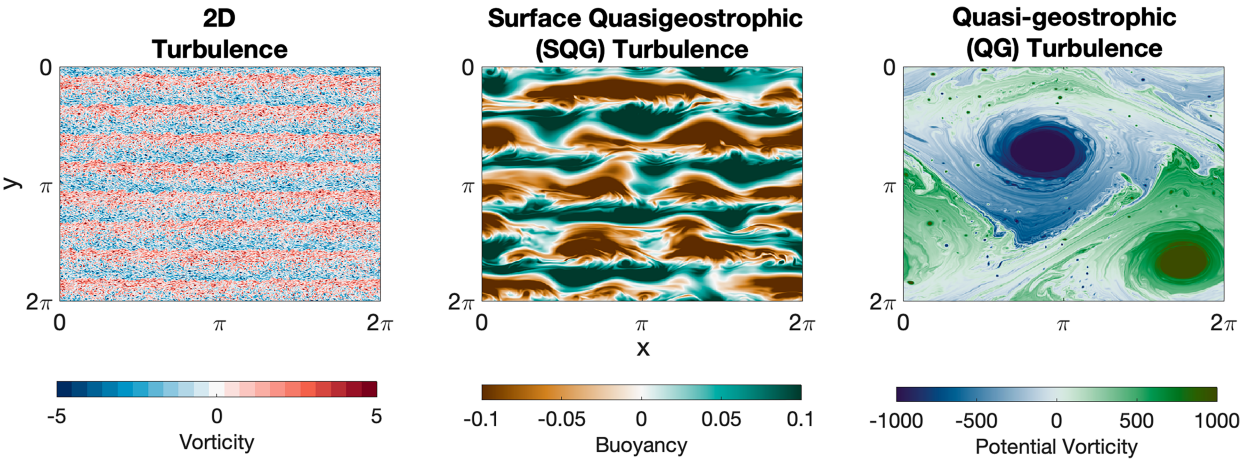

FIG. 1. Flow field from the final snapshot of each simulation. (left) Vorticity ω in 2D turbulence. (center) Buoyancy b in SQG turbulence. (right) QG potential vorticity q in the upper layer of two-layer QG turbulence.

with either 2048 × 2048 (2D) or 512 × 512 (QG and SQG) evenly spaced grid points, and are made anisotropic through the inclusion of β terms representing the background vorticity gradient (2D and QG turbulence) or background buoyancy gradient (SQG turbulence).

The simulated 2D turbulence creates a turbulent flow with zonal jets of alternating-signed vorticity (Fig. 1a). This simulation is forced within a narrow wavenumber band centered at $K_f = 100$, and dissipated via hyperviscosity at small scale, and by hypoviscosity at large scales ($D_{2d} = -\nu\nabla^8\omega + \mu\nabla^{-2}\omega$, where $\nu = 10^{-21}$ and $\mu = 0.044$). This creates an inverse energy cascade below K_f and a downscale enstrophy cascade above K_f (see Fig. 3). The anisotropy of the simulation is created through $\beta_{2d} = 10$. The presence of β_{2d} essentially makes this 2D system geophysically equivalent to a QG system with an infinite deformation radius. The analysis below utilizes 60 flow snapshots spread over several eddy turnover times once the system reaches forced-dissipative equilibrium. The 2D simulations are described in more detail in Pearson et al. (2021).

The simulated SQG turbulence also shows strong anisotropy through the creation of zonal jets, with alternating-signed buoyancy fluctuations (Fig. 1b). This simulation mimics the isotropic system that was simulated and detailed in Capet et al. (2008), although here we simulate a strongly anisotropic system through the inclusion of a large-scale buoyancy gradient via $\beta_{sqg} = 0.5$ (Smith et al. 2002; Lapeyre 2017). The forcing is narrowly centered at wavenumber $K_f = 7$, with hyper- and hypoviscosity ($D_{sqg} = -\nu\nabla^8 b + \mu\nabla^{-2} b$, where $\nu = 10^{-17}$ and $\mu = 0.005$). This produces a turbulent flow that cascades buoyancy variance to wavenumbers greater than K_f with a constant flux, while also transferring kinetic energy (KE) upscale with a flux that increases with decreasing wavenumber. The SQG system reaches a forced-dissipative equilibrium, and the analysis utilizes 62 distinct flow snapshots.

The simulated QG turbulence utilizes a two-layer QG system governed by Eq. (9). This simulation creates large eddies (Fig. 1c) that periodically collapse, reenergizing the flow with small-scale turbulence which then reorganizes into large eddies (Fig. 5). While the snapshot does not look strongly anisotropic, the flow evolution (not shown) demonstrates that eddy advection and the flow collapse are anisotropic processes. The interaction between the two layers is mediated by the coefficients:

$$\Gamma_i = \frac{H}{L_d^2 H_i}. \tag{22}$$

Here, $(H_1, H_2) = (0.2, 0.8)$ are the layer depths, $H = H_1 + H_2 = 1$ is the total depth, and $L_d = 0.35$ is the deformation radius of this system (Vallis 2006).

The QG simulation has no explicit vorticity forcing ($F_{qg,i} = 0$), but there is an imposed horizontal velocity jump between the upper layer ($i = 1$) and the lower layer ($i = 2$) which drives baroclinic instability. This velocity jump is imposed through a mean zonal velocity/streamfunction in each layer $\overline{\psi}_i = U_i y$ with $U_1 = 0.5$ and $U_2 = 0$, which also contributes to a mean meridional potential vorticity gradient in each layer, e.g., $\Gamma_1(U_1 - U_2)$. Since U_i and the gradient of Q_i are orthogonal, the mean flow advection is linear. This introduces anisotropy by mean advection of the turbulent potential vorticity $q_i' = q_i - Q_i$ and through advection of the mean vorticity gradient by turbulent velocities. Anisotropy is also induced by a background planetary vorticity gradient $\beta_{qg} = 0.5$, resulting in a total mean potential vorticity gradient of, e.g., $\partial_y \overline{Q_1} = \beta_{qg} + \Gamma_1(U_1 - U_2)$. Damping is applied through a linear drag within the bottom layer ($D_{qg,1} = 0$ and $D_{qg,2} = -\mu\nabla^2\psi_2$). The following analysis of the QG simulation uses only the fluctuating fields q_i' and synthesizes data from 81 distinct flow snapshots following the initial spinup (Fig. 5a). Note that the QG simulation is conducted for a relatively short nondimensional time duration [100 vs 3000 (2D) and 30 000 (SQG)], which corresponds to its relatively large (nondimensional) flow speeds.

g. *Calculating structure functions, spectral fluxes, and Bessel method integrals*

Structure functions and spectral fluxes are calculated through a combination of FluidSF (Wagner et al. 2024), which is an

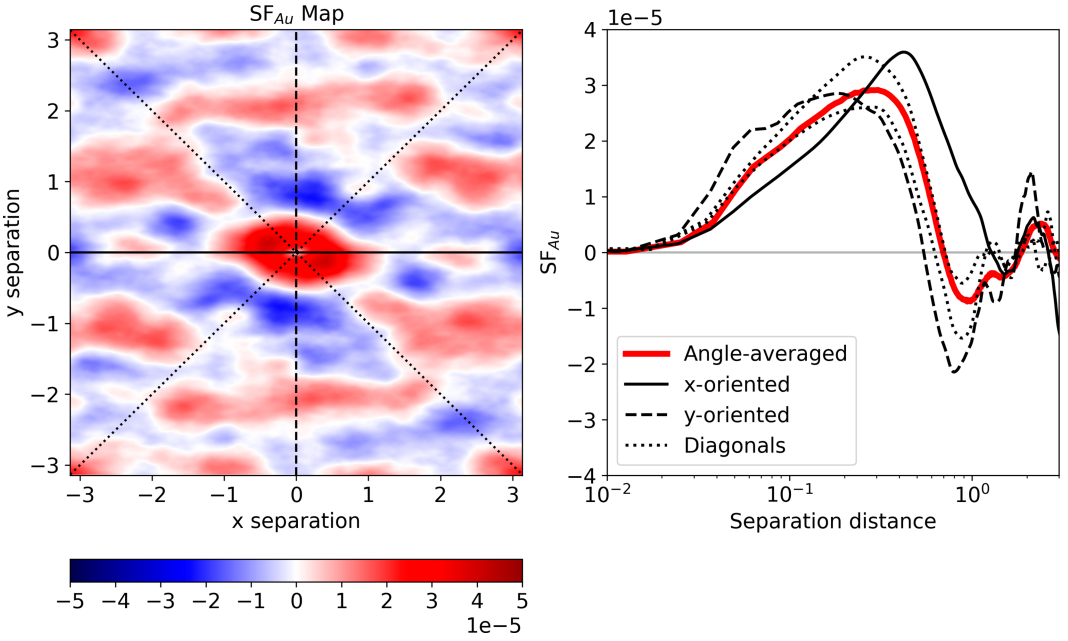

FIG. 2. Directional variation (anisotropy) of the advective velocity SF (SF$_{\mathcal{A}u}$) in the SQG simulation. (a) 2D maps of SF$_{\mathcal{A}u}$ time averaged across all snapshots and (b) a comparison between the angle-averaged version $\widetilde{\mathrm{SF}}_{\mathcal{A}u}$ and SFs calculated in four specific separation directions. The zonal, meridional, and diagonal lines in (a) correspond to the SFs plotted in (b).

open-source Python package for calculating spatial structure functions in 1D, 2D, and 3D systems (Wagner et al. 2025, manuscript submitted to *J. Open Source Software*), alongside in-house code (Pearson 2025). For each simulation, spectral fluxes and structure functions are calculated for several evenly spaced snapshots of the flow field. In the following analyses, we compare the time-averaged spectral fluxes against the fluxes estimated from time-averaged structure functions.

The new relations presented above [Eqs. (14), (17), (18), (21), and (20)] rely on angle-averaged structure functions (e.g., $\widetilde{\mathrm{SF}}_{\mathcal{A}u}$). However, it is computationally expensive to calculate all possible $\mathbf{r}$ orientations in large datasets, and this information is often not available from oceanic data. In anisotropic flows, the structure functions are also anisotropic, as seen in the SQG simulation (Fig. 2a) where the structure functions are zonally elongated, analogous to the jets that form in the SQG system (Fig. 1b). This means that using a single separation direction to calculate SF$_{\mathcal{A}u}$ may not provide an accurate estimate of $\widetilde{\mathrm{SF}}_{\mathcal{A}u}$ or the spectral fluxes. In the following analyses, four distinct structure functions are calculated for every dataset, each using a different separation (or sampling) direction: x-oriented $\mathbf{r} = (r, 0)$, y-oriented $\mathbf{r} = (0, r)$, and two diagonals $\mathbf{r} = (r/\sqrt{2}, \pm r/\sqrt{2})$, analogous to the 2D analysis of Pearson et al. (2021). The spectral flux estimates are averaged over the four sampling directions to approximate the angle-averaged structure function result, while avoiding the computationally expensive calculations that arise from consideration of all possible $\mathbf{r}$ orientations. This unidirectional sampling within anisotropic flows also allows us to explore how sampling direction affects spectral flux estimates, which is an important consideration for ocean observations that are often along specific tracks. In the following analyses, we show spectral flux estimates derived from the mean of these four time-averaged structure functions, in addition to their standard deviation (see, e.g., Fig. 3).

There are also several numerical considerations that are important for the spatial gradient, spectral flux, and integral computations. All the numerical simulations use pseudospectral methods, where variables are evolved in Fourier space and are then Fourier transformed to provide a spatially gridded dataset. The spectral flux computations [Eq. (1)] are performed in the natural Fourier space of the system. The structure functions are computed using the spatial fields. For advective structure functions, spatial gradients are computed using a centered difference with a three-point stencil that incorporates the closest adjacent grid points. This introduces a source of numerical error in these calculated gradients, as the centered difference truncates high-order terms from the precise, spectrally defined gradients. On a related topic, Pearson et al. (2021) used the IR method to explore the sensitivity of advective structure function-based flux estimates to the stencil width, emulating data that do not resolve the smallest scales of the turbulent flow. They found that increased stencil width (lower effective resolution) did not significantly affect the flux estimates at scales above the new effective resolution. The Bessel method integrations are performed using the cumulative trapezoidal method, creating another source of numerical error through the neglect of high-order terms. These numerical sources of error, combined with the directional subsampling and

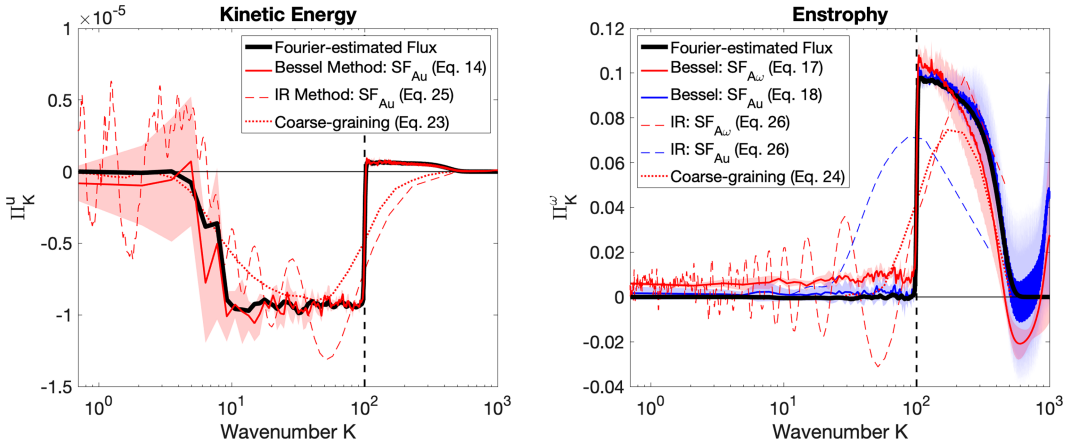

FIG. 3. Estimating spectral fluxes of (left) KE Π^u_K and (right) enstrophy Π^ω_K in anisotropic 2D turbulence. Comparison of the actual fluxes (black lines), flux estimates derived from the new Bessel methods [other solid lines; Eqs. (14), (17), and (18)], and flux estimates derived from IR methods [dashed lines; Eqs. (25) and (26)] or coarse graining [dotted lines; Eqs. (23) and (24)]. The shading around the Bessel method lines shows the standard deviation across the four sampled separation directions (i.e., uncertainty due to anisotropy of statistics), following the method described in section 2g. The IR method line here uses a single sampling direction, but all data are shown in appendix B. The forcing wavenumber is denoted by the vertical dashed black line.

averaging, crudely emulate typical oceanic datasets that sample a subset of flow field data and contain uncertainties. For this reason, we do not expect the mathematically precise relation such as Eq. (14) to hold perfectly in the following analyses. Future practice will surely improve on the numerical choices made here.

h. *Coarse graining*

To contrast the utility of the new SF methods against other existing methods, spectral fluxes are also estimated using coarse graining which is a method that is frequently used to estimate fluxes from gridded oceanic datasets (e.g., Aluie et al. 2018; Aluie 2019; Garabato et al. 2022; Storer et al. 2022; Contreras et al. 2023; Storer and Aluie 2023; Delpech et al. 2024). This method relies on the calculation of coarse-grained scalar fields [generically $f_\ell(\mathbf{x})$], defined as the convolution of the original field f and a low-pass filtering kernel G_ℓ which in our case is a top-hat function of width ℓ. Following Aluie et al. (2018), the downscale flux of energy through the length scale ℓ is then estimated from the correlation between strain and subfilter stress tensors:

$$\mathrm{Flux}^u_{\mathrm{cg}}(\ell) = -([uu]_\ell - u_\ell u_\ell)\frac{\partial u_\ell}{\partial x} - ([uv]_\ell - u_\ell v_\ell)\left(\frac{\partial v_\ell}{\partial x} + \frac{\partial u_\ell}{\partial y}\right) - ([vv]_\ell - v_\ell v_\ell)\frac{\partial v_\ell}{\partial y}. \quad (23)$$

The coarse-graining method is also used to estimate fluxes of scalar variances in analogy with the enstrophy flux method of Rivera et al. (2014) where we can replace ω with b or q:

$$\mathrm{Flux}^\omega_{\mathrm{cg}}(\ell) = -([u\omega]_\ell - u_\ell\omega_\ell)\frac{\partial \omega_\ell}{\partial x} - ([v\omega]_\ell - v_\ell\omega_\ell)\frac{\partial \omega_\ell}{\partial y}. \quad (24)$$

All of the coarse-grained fluxes are a function of length scale ℓ associated with the filtering kernel. The coarse-grained fluxes are calculated for 25 length scales ℓ, which are mapped to wavenumber space using a nominal conversion $\mathrm{Flux}^\phi_{\mathrm{cg}}(\ell) \to \Pi^\phi_{\mathrm{cg}}(K = \pi/\ell)$. Note we choose not to use the standard space-to-wavenumber conversion $[(2\pi/\ell) \to K]$ for coarse-graining fluxes to provide the best match with the Fourier-estimated fluxes, but unlike for structure function conversions (section 2g), we do not propose a physical justification for the coarse-graining conversion factor here.

It is important to note that the coarse-graining flux is not identical to the spectral flux, since coarse graining uses a kernel that is localized in real space, while the spectral flux effectively uses a kernel that is localized in Fourier space (Aluie et al. 2018). However, given the complete flow data available in these numerical simulations with doubly periodic boundary conditions, we anticipate that the coarse-graining and spectral fluxes should have comparable relative magnitudes and signs (flux directions) at a given scale. The approximate real-to-Fourier space remapping means the location of peaks and flux direction changes may not be perfectly aligned.

3. Results

a. *Two-dimensional (2D) turbulence: Spectral fluxes of energy and enstrophy*

In the 2D turbulence simulation, there are several interesting spectral fluxes. At the largest scales or smallest wavenumbers ($K < K_f = 100$), there is an inverse energy cascade where $\Pi^u_K < 0$ moves energy to larger scales (Fig. 3a). At smaller scales or larger wavenumbers ($K > K_f$), there is a downscale enstrophy cascade where Π^ω_K moves enstrophy to smaller scales ($K > K_f$; Fig. 3b) and a coincident subdominant spectral flux of energy to smaller scales (Fig. 3a).

Equations (14), (17), and (18) accurately capture all of the fluxes in the 2D turbulence simulation, including the sharp flux transition at the forcing wavenumber K_f and the downscale energy flux at the highest wavenumbers. The enstrophy cascade can be diagnosed from both the velocity-based advective structure functions, in addition to its vorticity-based counterpart [Eqs. (17) and (18)]. This could be beneficial for datasets where taking additional gradients of the flow fields is not desired.

The new Bessel methods [Eqs. (14), (17), and (18)] are also contrasted against IR methods proposed in Pearson et al. (2021) to estimate fluxes of energy Π^u_K and enstrophy Π^ω_K:

$$\Pi^u_K \approx -\mathrm{SF}_{\mathcal{A}u}/2, \tag{25}$$

$$\Pi^\omega_K \approx \begin{cases} -\mathrm{SF}_{\mathcal{A}\omega}/2, \\ 2\mathrm{SF}_{\mathcal{A}u}/r^2, \end{cases} \tag{26}$$

in addition to the coarse-graining flux estimates. The Bessel methods [Eqs. (14), (17), and (18)] diagnose the dominant cascades more accurately than proportional relationships [Eqs. (25) and (26)] and coarse graining [Eqs. (23) and (24)]. The Bessel methods also have the benefit that they uniquely capture the subdominant flux (downscale energy at $K > K_f$) and the sharp transition of spectral fluxes at the forcing scale. It is notable that the Bessel method captures the downscale (positive) flux at high wavenumbers, despite the advective structure function being single signed across the wavenumber range spanning downscale and inverse energy fluxes, as seen by the IR method (red dashed line in Fig. 3a) being negative for $K > 10$. This suggests that the Bessel method integral at large K is being dominated by the contributions from negative lobes of the Bessel function for $Kr \gg 1$ (Fig. A1), where $\mathrm{SF}_{\mathcal{A}u}$ is increasing with r or equivalently the IR method becomes more negative as K decreases.

b. *SQG turbulence: Spectral fluxes of kinetic energy and buoyancy variance*

The SQG system has several properties that make it an interesting test for the methods proposed in Eqs. (14) and (20). In SQG turbulence, the power spectrum of kinetic energy E_K is identical to the power spectrum of buoyancy variance $E^b_K = \widehat{|b|}^2/2$, which also means the second-order structure functions of velocity $\overline{\delta\mathbf{u}\cdot\delta\mathbf{u}}$ and buoyancy $\overline{\delta b\delta b}$ are identical. However, the momentum and buoyancy fields, and their tendency equations, are not identical. The spectral fluxes of the two power spectra are also different, as seen in their budgets (Capet et al. 2008):

$$\frac{\partial E^b_K}{\partial t} = -\mathrm{Re}\{\widehat{\mathbf{u}}^*\widehat{(\mathbf{u}\cdot\nabla)b}\}, \tag{27}$$

$$\frac{\partial E_K}{\partial t} = \underbrace{-\mathrm{Re}\{\widehat{\mathbf{u}}^*\widehat{(\mathbf{u}\cdot\nabla)\mathbf{u}}\}}_{\Pi^u_K\text{-related term}} - \underbrace{\mathrm{Re}\left\{\widehat{\frac{\partial w}{\partial z}}\widehat{\psi}\right\}}_{\text{Ageostrophic term}}, \tag{28}$$

where we have neglected forcing, dissipation, and β_{sqg} terms for simplicity. Given that $E^b_K = E_K$ in the SQG system, it follows that the right-hand sides of Eqs. (27) and (28) must be identical. Both systems include advection by the surface velocity field $\mathbf{u}$, which creates the spectral fluxes Π^u_K and Π^b_K that Eqs. (14) and (20) aim to diagnose. However, the kinetic energy budget [Eq. (28)] also contains a term that depends on the vertical velocity w gradient. In this system, the fluid is incompressible and $\mathbf{u} = (-\psi_y, \psi_x)$ is a geostrophic (nondivergent) velocity field, so this new term represents the effects of a horizontally divergent ageostrophic flow. This ageostrophic flow arises from the vertical derivatives of the streamfunction via the buoyancy definition and the constraint of zero interior potential vorticity, and within the SQG system, it only affects the momentum budget. The ageostrophic term moves kinetic energy between scales and is comparable in magnitude to the spectral fluxes, which means that Π^u_K and Π^b_K can be different (see Fig. 4) despite the equivalence of their underlying power spectra.

In the SQG simulation, there is a downscale cascade of (surface) buoyancy variance below the forcing scale (Fig. 4b) and a coincident upscale flux of kinetic energy toward the forcing scale that increases closer to the forcing scale (Fig. 4a). At the smallest scales, there is also a subdominant downscale flux of energy. The new methods proposed in Eqs. (14) and (20) capture the spectral fluxes of both kinetic energy and buoyancy variance in this system, including the upscale-to-downscale transition of the kinetic energy flux at small scales. These methods are contrasted against proportional relationships for the fluxes of kinetic energy [Eq. (25)] and of buoyancy variance:

$$\Pi^b_K \approx -\mathrm{SF}_{\mathcal{A}b}/2, \tag{29}$$

in addition to coarse-graining flux estimates. The proportional relationships and coarse graining provide reasonable estimates of the spectral fluxes but with less accuracy (magnitude and wavenumber resolution) than the Bessel methods and without capturing the downscale energy flux at high wavenumbers.

c. *QG turbulence: Spectral fluxes of kinetic energy, potential enstrophy, and enstrophy*

The QG simulation does not reach a steady equilibrium state (Fig. 5). The simulation spends most of its time in a state of decaying kinetic energy, where large-scale, coherent eddies exist in a sea of small-scale turbulence (e.g., Fig. 5c). However, the system periodically collapses into a state of small-scale turbulence without large, coherent eddies (e.g., Fig. 5b), followed by a rapid reenergization of the system. This provides a test of whether the Bessel methods [Eqs. (14), (21), and (17)] can diagnose time-mean spectral fluxes in a transient/nonstationary system, which is critical for measuring the time-averaged energy cycle/budgets. In the following analyses, we will compare time-averaged fluxes with estimates from time-averaged structure functions, and we will confine our analysis to the top layer of the model, which is analogous to the systems we are likely to observe at the ocean surface where most observations are located.

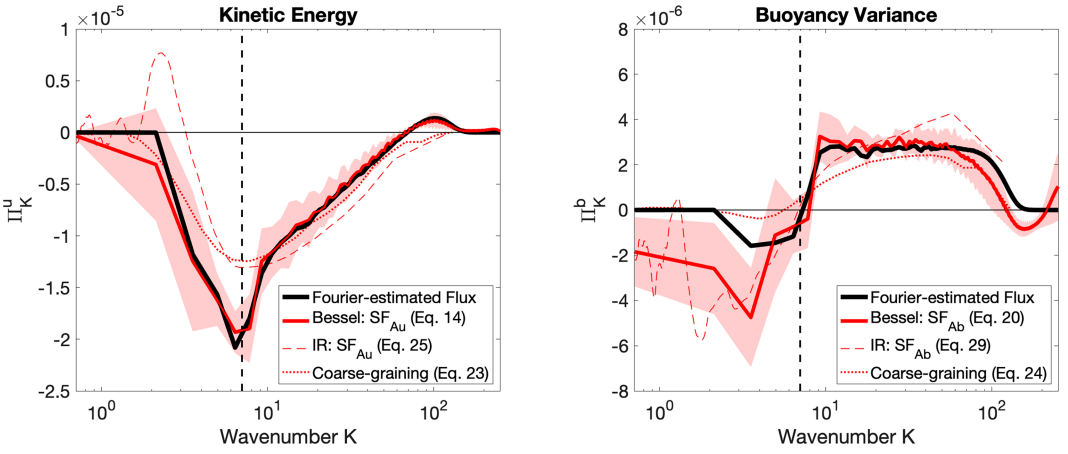

FIG. 4. Estimating spectral fluxes of (left) KE Π_K^u and (right) buoyancy Π_K^b in anisotropic SQG turbulence. Analogous to Fig. 3 with actual fluxes, flux estimates derived from the new Bessel methods [Eqs. (14) and (20)] and flux estimates derived from IR methods [Eqs. (25) and (29)] or coarse graining [Eqs. (23) and (24)]. The forcing wavenumber is denoted by the vertical dashed black line.

At scales larger than the deformation radius ($K < k_d$), there is a spectral flux of kinetic energy to larger scales (Fig. 6a), while at scales smaller than the deformation radius ($K < k_d$), there is a downscale spectral flux of enstrophy (Fig. 6c) alongside a smaller downscale flux of kinetic energy (Fig. 6a). At all wavenumbers, there is a flux of potential enstrophy Π_K^q to smaller scales (Fig. 6b). The large-scale (small-K) potential enstrophy flux is driven by the layer interaction component of $q_1 = \omega_1 + \Gamma_1(\psi_2 - \psi_1)$, while the smaller-scale Π_K^q is dominated by the enstrophy dynamics based on the similarity of Figs. 6b and 6c for $K \gg K_d = 2\pi/L_d$.

The Bessel methods proposed in Eqs. (14), (21), (17), and (18) generally capture the spectral fluxes of kinetic energy, potential enstrophy, and enstrophy in the QG system. The main differences are that the potential enstrophy estimates are slightly larger than the actual flux Π_K^q, and the enstrophy flux estimate from $\widetilde{\mathrm{SF}}_{\mathcal{A}\omega}$ underestimates the small-scale extent of the spectral flux of enstrophy Π_K^ω. Both estimates of Π_K^ω also erroneously predict a small downscale spectral flux at large scales. We compare these methods to the proportional relations for kinetic energy [Eq. (25)], enstrophy [Eq. (26)], and potential enstrophy:

$$\Pi_K^q \approx -\mathrm{SF}_{\mathcal{A}q}/2, \tag{30}$$

in addition to coarse-graining flux estimates. Consistent with the SQG results, the proportional relationships and coarse graining provide reasonable estimates of the spectral fluxes in QG turbulence but with less accuracy (magnitude and wavenumber resolution) than the Bessel methods and without capturing the downscale energy flux at small scales. The exception is that coarse graining more accurately captures the magnitude of the downscale potential enstrophy flux, which is overestimated by the structure function-based methods.

Both the Bessel method and the IR method overestimate the downscale potential enstrophy flux in Fig. 6b. To identify potential causes of this flux overestimation, the distinct structure function characteristics and dynamics of potential enstrophy in the

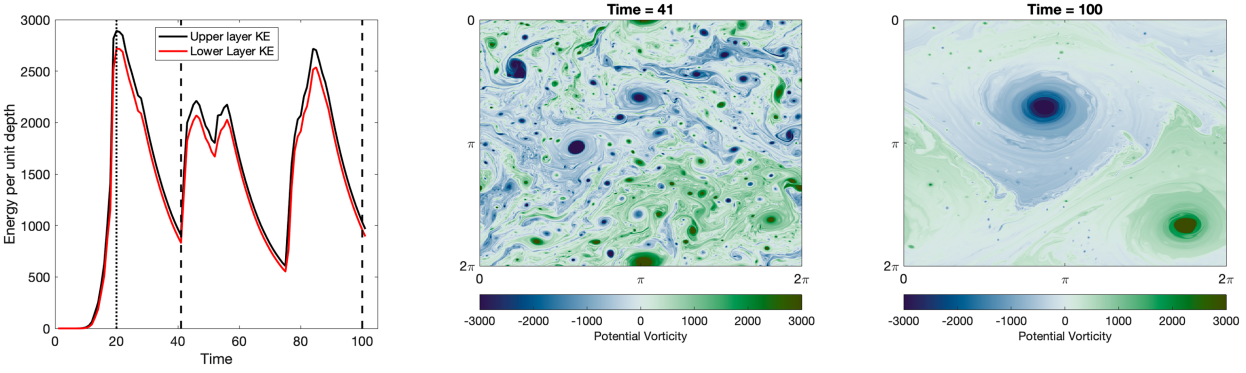

FIG. 5. Visualizing the nonstationarity of the QG system. (left) Depth-normalized KE within each layer as a function of time, with dashed lines indicating (center),(right) the time of the potential enstrophy snapshots. The vertical dotted line indicates the earliest snapshot used for SF and spectral flux calculations for the QG system.

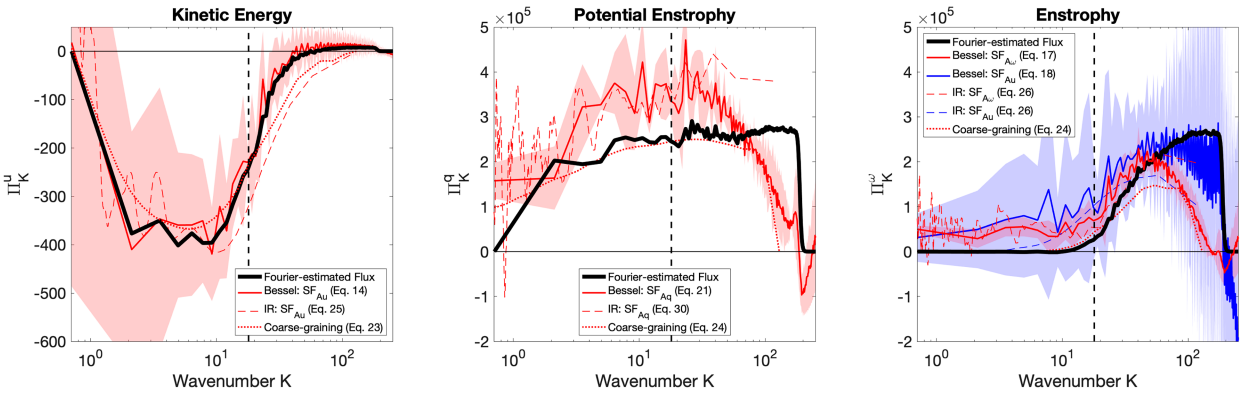

FIG. 6. Estimating spectral fluxes of (left) KE Π_K^u, (center) QG potential enstrophy Π_K^q, and (right) enstrophy Π_K^ω in anisotropic two-layer QG turbulence. Analogous to Fig. 3 with actual fluxes, flux estimates derived from the new Bessel methods [Eqs. (14), (17), (18), and (21)] and flux estimates derived from IR methods [Eqs. (25), (26), and (30)] or coarse graining [Eqs. (23) and (24)]. The deformation wavenumber $K_d = 2\pi/L_d$ is denoted by the vertical dashed black line.

QG system must be discussed and contrasted against the scalar fluxes in 2D and SQG turbulence which do not show this issue. First, the potential enstrophy advective structure function is large at both the small- and large-scale extents of the data (red dashed line in Fig. 6b). This structure function signal could be due to the numerical computation of gradients or the presence of large-scale imposed gradients through β terms. This behavior is seen at either the small or large scales (but not both) for the scalars across all systems using the IR method (red dashed lines): vorticity in 2D turbulence (Fig. 3b) and buoyancy in SQG turbulence (Fig. 4b). Second, the potential vorticity is a combination of both relative vorticity and stretching terms in $q_1 = \omega_1 + \Gamma_1(\psi_2 - \psi_1)$, which results in additional dynamics versus other scalars investigated through the associated layer interaction and vertical fluxes that are not explored here. Finally, the extent of the potential enstrophy spectral flux spans all wavenumbers in contrast to the buoyancy and (relative) vorticity fluxes studied here, which are confined to the smallest scales or largest wavenumbers in each system.

We hypothesize that the above factors combine in this simulated QG turbulence to create advective structure functions with an additional background factor which is observed at small-K plateau of $\mathrm{SF}_{\mathcal{A}\omega}$ that estimates $\Pi_K^\omega \approx 5 \times 10^4$ (red dashed line in Fig. 6c) despite no vorticity flux at these scales, and in the large-K stretching-associated advective structure function $(\mathrm{SF}_{\mathcal{A}q} - \mathrm{SF}_{\mathcal{A}\omega})$, not shown but inferrable from Figs. 6b,c) which estimates $(\Pi_K^q - \Pi_K^\omega) \approx 7 \times 10^4$ despite the flux being entirely driven by relative vorticity at these scales (cf. black lines in Figs. 6b,c). A more detailed investigation of the potential enstrophy dynamics of multilayer β-affected QG turbulence and the implications for potential vorticity flux estimation is left to a future study.

d. *Effects of limited sampling range or resolution*

Estimating spectral fluxes through Eqs. (14), (17), (18), (20), and (21) requires integration of functions over all possible separation distances. In reality, structure functions have a limited range and resolution, so these spectral estimates would take the form

$$\Pi_K^u \approx \int_{r_{\min}}^{r^{\max}} f(K, r)dr, \tag{31}$$

where $r_{\min}$ and $r_{\max}$ represent the smallest and largest calculable separation distances, respectively, and the form of $f(K, r)$ depends on the flux being estimated and the structure function being used [e.g., Eqs. (14), (15), (17), or (18)]. In the above analyses, $r_{\min} = \Delta$ was the resolution of the simulation grid Δ, while $r^{\max} = L/2$ was half the domain extent L. In doubly periodic systems, this range of r encompasses all the dynamics of the system.

To investigate how a limited range of separation distances affects spectral flux estimates, we recompute the spectral flux estimates using Eq. (31) with artificial limits on either separation distance extent $r_{\max}$ or resolution $r_{\min}$. To capture the effects of range limits that occur at scales with differing turbulent dynamics (i.e., located in different cascades), we explore the effects of $L/r_{\max} = (8, 16, 32, 64)$ and $r_{\min}/\Delta = (2, 4, 8, 16)$. Flux estimates from truncated datasets are compared against the Fourier-estimated fluxes using the full datasets, but a crude dimensional estimate that does not account for the nonlocality of real-to-Fourier-space conversion would suggest that in a best-case scenario the truncated data would likely provide information only about wavenumbers $2\pi/r_{\max} < K < \pi/r_{\min}$.

Spectral flux estimates are affected by changes in the minimum resolved separation distance $r_{\min}$, but these effects are confined to the smallest scales or highest wavenumbers (Fig. 7). For each value of $r_{\min}$, dashed vertical lines show the corresponding maximum resolved wavenumber $K_{\max}$ estimated from the Bessel function peak (see section 2e for details), and structure functions are only shown for wavenumbers below $K_{\max}$. In general, changing $r_{\min}$ only impacts the flux estimates from roughly $K_{\max}/2 \rightarrow K_{\max}$. Estimates of energy, enstrophy, and buoyancy variance fluxes outside this range are accurate in all the systems, indicating that fluxes can be measured provided

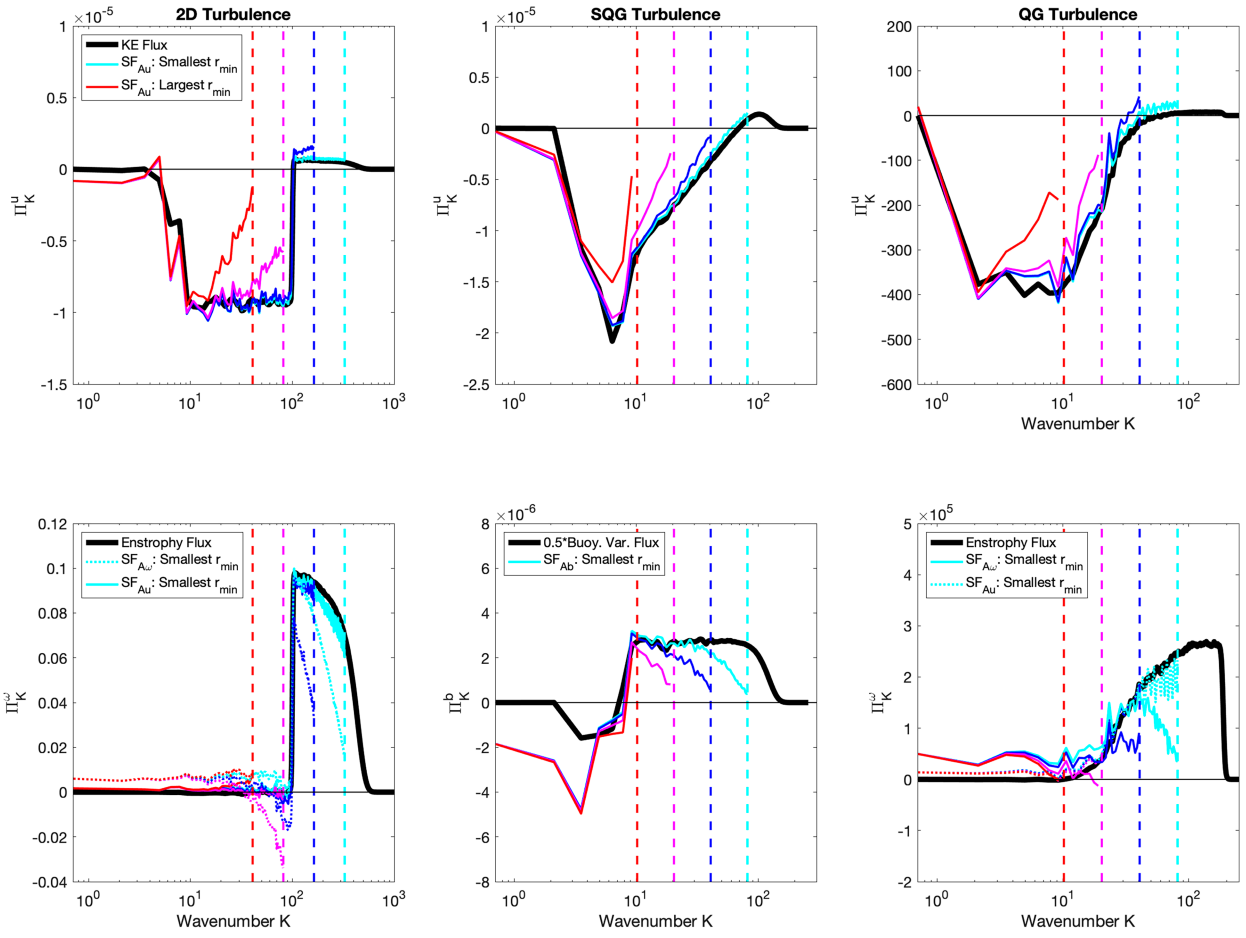

FIG. 7. Impact of limited separation distance resolution $r_{\min}$ on spectral flux estimates in 2D, SQG, and multilayer QG turbulence.

the spatial resolution of data is several times smaller than the scale at which the flux of interest is occurring.

Spectral flux estimates are also affected by changes in the maximum measured separation distance $r_{\max}$, but in many cases these effects do not change flux estimates at the smallest length scales or highest wavenumbers (Fig. 8). For each value of $r_{\max}$, dashed vertical lines show the corresponding minimum resolved wavenumber $K_{\min}$ estimated from the Bessel function peak (see section 2e for details), and structure functions are only shown for wavenumbers above $K_{\min}$. In general, reducing $r_{\max}$ introduces oscillatory behavior in the flux estimates. Despite these oscillations, advective velocity structure functions are still able to diagnose inverse energy fluxes even when $r_{\max}$ lies within this inverse flux region. In the two-layer QG system, estimates of the potential enstrophy flux are also affected by $r_{\min}$ and $r_{\max}$ (not shown), showing similar behavior to the energy fluxes with oscillations near $r_{\max}$ or $K_{\min}$ and a rolloff near $r_{\min}$ or $K_{\max}$.

The downscale fluxes of enstrophy (2D and QG systems) and buoyancy variance (SQG system) can also be diagnosed from their respective advective structure functions, even when $r_{\max}$ is small (i.e., you do not need to resolve large-scale dynamics to measure small-scale fluxes). The biggest impact of limited $r_{\max}$ is through the small-scale (large-K) oscillations of flux estimates based on the advective velocity structure function. This manifests in the $\mathrm{SF}_{\mathcal{A}u}$ estimates of the enstrophy cascade and to a lesser extent the downscale energy cascade of 2D turbulence. This is consistent with $\mathrm{SF}_{\mathcal{A}u}$ having the largest magnitude at large scales or small wavenumbers (e.g., dashed lines on left panels of Figs. 3, 4, and 6), so missing this significant component of the $\mathrm{SF}_{\mathcal{A}u}$ signal when large scales are omitted degrades the accuracy of its derived flux estimates.

e. *Comparing advective and third-order structure function methods for flux estimation*

The present study also provides an opportunity to contrast flux-estimation methods that utilize recently proposed advective structure functions against analogous methods that utilize third-order structure functions, which have been applied in previous studies. Appendix B presents Bessel method relations for estimating energy fluxes using third-order structure functions of velocity [SF_{Luu}, Eq. (B3); SF_{LLL}, Eq. (B4)] and for estimating scalar-variance fluxes such as enstrophy from their third-order structure functions [$\mathrm{SF}_{L\omega\omega}$, Eq. (B9)]. The IR method for estimating energy and scalar variances from third-order structure functions is summarized in Table 1 of

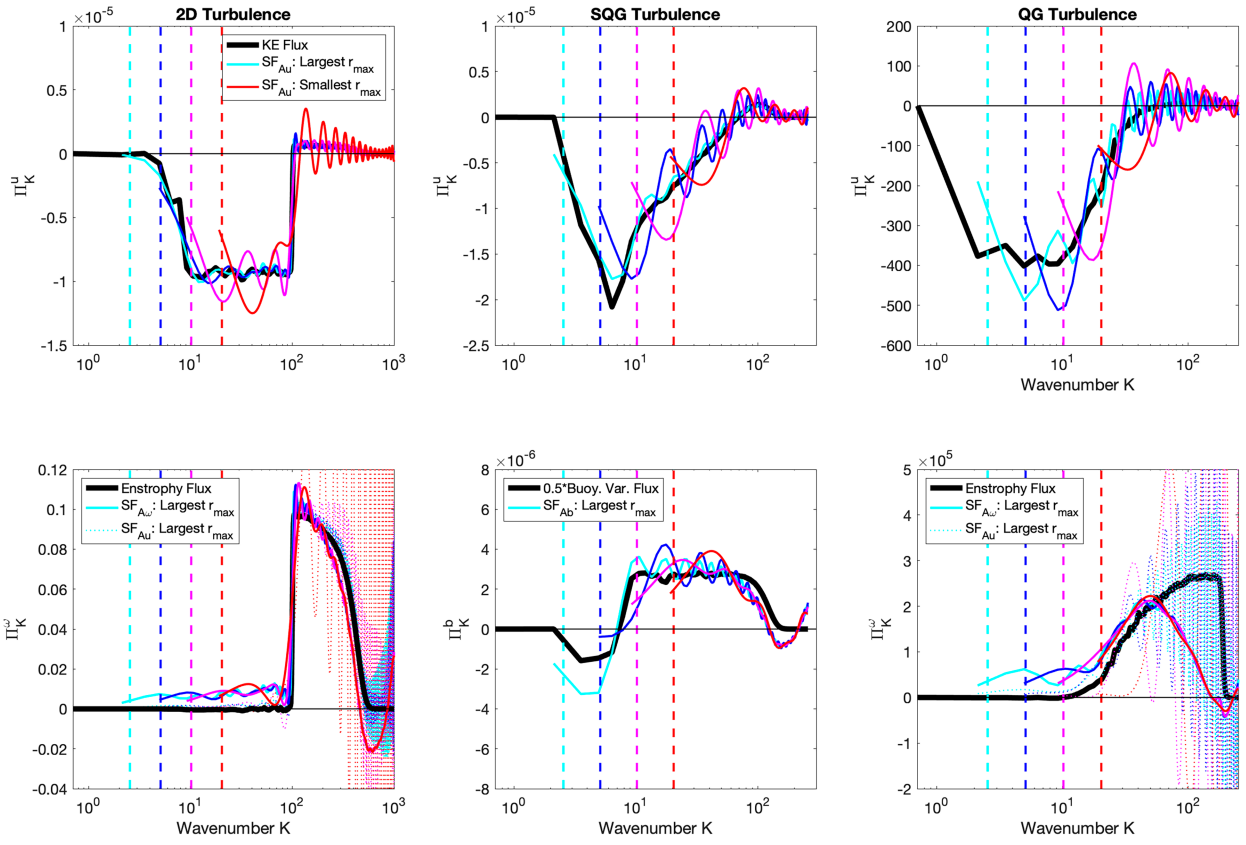

FIG. 8. Impact of limited separation distance extent $r_{\max}$ on spectral flux estimates in 2D, SQG, and multilayer QG turbulence.

Pearson et al. (2021). Figures B1–B3 contrast the various methods for estimating energy and scalar-variance fluxes (black lines) in all the simulated systems using different structure functions and using Bessel methods (red lines) or IR methods (blue lines). These comparisons will be discussed in the remainder of this section, but the figures are located within the appendix due to their high information density.

For energy flux estimation, the advective structure functions are more isotropic than third-order structure functions (Figs. B1–B3, upper panels). Third-order velocity structure functions show significant dependence on the separation direction being sampled, while advective velocity structure functions are relatively agnostic to sampling direction (blue lines). This anisotropy also propagates to the Bessel method energy flux estimates (red lines). For the Bessel method flux estimates, there is also an increase in noise for methods that require higher-order Bessel functions and additional integration by part terms, with the lowest noise for $\mathrm{SF}_{\mathcal{A}u}$ and a very large amount of noise for SF_{LLL}. None of the third-order velocity structure function methods capture the small downscale energy transfer at the highest wavenumbers in the three systems consistently across sampling directions.

The enstrophy flux estimates in 2D and two-layer QG turbulence (Figs. B1 and B3, lower panels) show a similar behavior to the energy flux estimates. The IR and Bessel methods based on the third-order vorticity structure function $\mathrm{SF}_{L\omega\omega}$ produce enstrophy flux estimates that are more anisotropic than the analogous advective structure function methods using $\mathrm{SF}_{\mathcal{A}u}$ or $\mathrm{SF}_{\mathcal{A}\omega}$. Within SQG turbulence, both advective and third-order structure functions produce accurate and anisotropic estimates of the downscale flux of buoyancy variance (Fig. B2, lower panels). The noise increase that was present in the energy flux estimates from advective to third-order structure function methods is not present for enstrophy and buoyancy variance flux estimates, suggesting that the accuracy of different-order Bessel function methods may depend on the type, direction, and/or dominant scales of the spectral flux being diagnosed. We leave a more rigorous investigation of these properties to future work.

4. Conclusions

Several new methods were proposed to estimate spectral fluxes in quasi-2D systems such as large-scale ocean or geophysical dynamics [Eqs. (14), (17), (18), (20), and (21)]. These Bessel methods integrate the product of advective structure functions and Bessel functions to estimate spectral fluxes of dynamically important quantities. This method was validated in a range of numerically simulated strongly anisotropic geophysical turbulence, including nonstationary dynamics and other complex systems. The present analyses emulate realistic datasets with errors and subsampling (section 2g), providing a

robustness test for the theoretically exact Bessel methods relating structure functions and angle-averaged advective structure functions computed from complete flow fields [e.g., Eq. (14)]. The new methods were shown to have several benefits over other common flux-estimation methods (coarse-graining and inertial-range methods based on structure function proportionality relations). An analogous integration method was proposed to estimate the inverse energy cascade in 2D turbulence using third-order velocity-based structure functions (Xie and Bühler 2018), but the advective structure function integration methods are less noisy and less impacted by flow anisotropy than the third-order structure function integration methods (appendix B). The present analysis of doubly periodic systems allows direct computation of spectral fluxes alongside flux-estimation methods. These flux-estimation methods are critical tools for inferring fluxes in more complex datasets where spectral fluxes cannot be calculated.

The new Bessel methods diagnosed spectral fluxes of energy to larger and smaller scales (validated in 2D, QG, and SQG systems) in addition to the downscale fluxes of enstrophy (2D) and buoyancy variance (SQG). The new method provides more accurate estimates of the upscale spectral fluxes of energy and the abovementioned downscale fluxes when compared to existing structure function methods and coarse graining. The new method is also unique in its ability to diagnose downscale energy fluxes at small scales in 2D, SQG, and QG turbulence, scale-varying fluxes such as the kinetic energy fluxes in QG and SQG turbulence (which become larger at smaller wavenumbers), and flux-transition scales that are associated with forcing or instability scales. These properties are critical to quantify the contribution of mesoscale dynamics to the oceanic energy cycle, where flow is dynamically complex and energy is anticipated to be transferred to both larger (gyre) scales and smaller (submesoscale) motions (Balwada et al. 2022). Although the analysis here was conducted using reduced-dynamics models, these dynamics apply over a range of scales spanning the mesoscale to the submesoscale. As a result, the new diagnostic methods can be applied to general data at these scales (e.g., mesoscale observations or primitive equation models). The Bessel method overestimates the downscale flux of potential enstrophy in QG turbulence, although the cause of this difference is still an open question.

The Bessel methods theoretically require integrals over separation distances $0 \leq r \leq \infty$, which is not practical for real data. Sensitivity studies indicate that even with a limited range of measured scales (r), spectral fluxes can be diagnosed at wavenumbers within the span of separation distances measured, provided an appropriate inversion from distance to wavenumber is used ($K \propto r^{-1}$; see section 2e). Limited measurement range can induce oscillatory behavior in spectral flux estimates, particularly at high wavenumbers in methods using the advective velocity structure function and higher-order Bessel functions.

Advective structure functions require measurement of local gradients of flow fields. This information can be gleaned from two-dimensional field measurements (i.e., radar, modern satellite altimeters, simulation output), but this method may also be applicable to Lagrangian or in situ observations if methods are developed to estimate the advection operator (e.g., from Lagrangian acceleration or standing eddy hypotheses, respectively). However, even in situations where flow fields are measured but local advection cannot be estimated, it may still be possible to calculate traditional third-order structure functions and apply analogous Bessel methods such as those detailed in appendix B and in Xie and Bühler (2018, 2019). Datasets that are amenable to advective structure function analysis to estimate spectral fluxes are also likely to be suited for coarse-graining analysis. As we have shown, coarse-graining inferred fluxes often capture the inverse energy cascade across systems but do not capture the downscale transfer of energy at the small scales of these simulated systems that spectral fluxes and Bessel methods capture.

Acknowledgments. This material is based upon work supported by the National Science Foundation under Grant OCE-2023721. B. F.-K. was supported by the Department of Energy under Award DE-SC0024572.

Data availability statement. The code used to run simulations and analyze data for this manuscript is available through a public GitHub repository archived on Zenodo: Pearson (2025). While the simulation data are too large to share directly, the simulation files can be used to reproduce all the data used within this paper.

APPENDIX A

Heaviside Transformation in Two Dimensions

The relations presented in this work rely on applying the Plancherel theorem, relating products of real-space functions to the product of their wavenumber-space functions:

$$\int_{-\infty}^{\infty} f(x)g^*(x)dx = \int_{-\infty}^{\infty} \widehat{f(k)}\widehat{g}^*(k)dk, \tag{A1}$$

where g^* denotes the complex conjugate of g. This theorem generalizes to n-dimensional space and is used to convert the exact relation between the spectral flux and (Fourier-transformed) advective structure function,

$$\Pi_K^u = -\frac{1}{2}\int_{-\infty}^{\infty}\int_{-\infty}^{\infty} \widehat{(\mathrm{SF}_{\mathcal{A}u})} H(K-\kappa)dkdl, \tag{A2}$$

into a relation between the spectral flux and the real-space advective structure function:

$$\Pi_K^u = -\frac{1}{2}\int_{-\infty}^{\infty}\int_{-\infty}^{\infty} \mathrm{SF}_{\mathcal{A}u} F dxdy, \tag{A3}$$

where F is the inverse Fourier transform of the Heaviside function $\widehat{F} = H(K-\kappa)$. Note we also used the property that the Heaviside function and its transform are real functions (see below).

In this appendix, we derive F in a two-dimensional system. We start from the inverse transform relation:

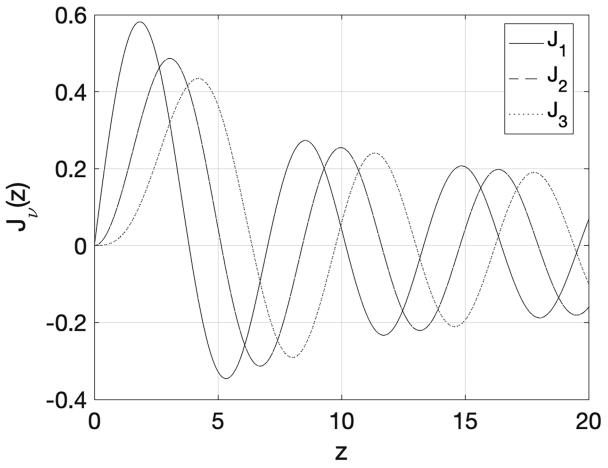

FIG. A1. Plots of the first-, second-, and third-order Bessel functions of the first kind.

$$F = \frac{1}{(2\pi)^2}\int_{-\infty}^{\infty}\int_{-\infty}^{\infty}\widehat{F}e^{i\mathbf{k}\cdot\mathbf{x}}dkdl, \tag{A4}$$

where $\mathbf{k} = (k, l)$ is the wavenumber vector. Transforming to polar coordinates in wavenumber space $(k, l) = (\kappa\cos\theta, \kappa\sin\theta)$ and real space $(x, y) = (r\cos\phi, r\sin\phi)$, we find

$$\begin{aligned} F &= \frac{1}{(2\pi)^2}\int_0^{\infty}\int_0^{2\pi}\widehat{F}\kappa e^{i\kappa r(\cos\theta\cos\phi+\sin\theta\sin\phi)}d\theta d\kappa \\ &= \frac{1}{(2\pi)^2}\int_0^{K}\int_0^{2\pi}\kappa e^{i\kappa r\cos(\theta-\phi)}d\theta d\kappa, \end{aligned} \tag{A5}$$

where we also now apply the Heaviside function as a constraint on the integral limits. Utilizing the Jacobi–Anger expansion $e^{iz\cos\phi} = \sum_{n=-\infty}^{\infty} i^n J_n(z)e^{in\phi}$,

$$F = \frac{1}{(2\pi)^2}\int_0^{K}\int_0^{2\pi}\kappa\left[\sum_{n=-\infty}^{\infty} i^n J_n(\kappa r)e^{in\theta}e^{-in\phi}\right]d\theta d\kappa. \tag{A6}$$

This expression can be noted that all integer $n \neq 0$ terms vanish when the angular integral is evaluated:

$$F = \frac{1}{(2\pi)^2}\int_0^{K}\int_0^{2\pi}\kappa J_0(\kappa r)d\theta d\kappa = \frac{1}{2\pi}\int_0^{K}\kappa J_0(\kappa r)d\kappa. \tag{A7}$$

Finally, a change in variables $\zeta = \kappa r$, and noting the Bessel function property $d[\zeta J_1(\zeta)]/dx = \zeta J_0(\zeta)$,

$$\begin{aligned} F &= \frac{1}{2\pi r^2}\int_0^{Kr}\zeta J_0(\zeta)d\zeta \\ &= \frac{1}{2\pi r^2}[\zeta J_1(\zeta)]_{\zeta=0}^{Kr} \\ &= \frac{K}{2\pi r}J_1(Kr). \end{aligned} \tag{A8}$$

Now that we have an expression for F, we can substitute this into Eq. (A3) to find

$$\Pi_K^u = -\frac{K}{4\pi}\int_{-\infty}^{\infty}\int_{-\infty}^{\infty}\mathrm{SF}_{Au}\frac{J_1(Kr)}{r}dxdy. \tag{A9}$$

The first-order Bessel function is zero when $K_r = 0$, positive for small Kr, and after reaching a maximum at $Kr \approx 2$ (Fig. A1), the function is oscillatory and as $(Kr)^{1/2}$ for large Kr (Abramowitz and Stegun 1948).

APPENDIX B

Derivation of Relations between Third-Order Structure Functions and Spectral Fluxes

In the main text, relations between spectral fluxes and advective structure function were presented. In this appendix, we derive the analogous relations between spectral fluxes and third-order structure functions. It has previously been shown that, in incompressible turbulence, the spectral flux of energy Π_K^u through a specific wavenumber K is related to the third-order velocity structure function [SF_{uuu}; Eq. (4)] through an integral transform (Frisch 1995):

$$\Pi_K^u = -\frac{1}{4}\iint(\widehat{\nabla\cdot\mathrm{SF}_{uuu}})H(K-\kappa)dkdl, \tag{B1}$$

where $H()$ is the Heaviside function and $\kappa = \sqrt{k^2+l^2}$. Using Plancherel's theorem, this can be converted to a real-space integral (Xie and Bühler 2018):

$$\begin{aligned} \Pi_K^u &= -\frac{1}{8\pi}\iint(\nabla\cdot\mathrm{SF}_{uuu})\frac{K}{r}J_1(Kr)dxdy = \\ &-\frac{K}{4}\int\frac{1}{r}\frac{\partial(r\mathrm{SF}_{Luu})}{\partial r}J_1(Kr)dr, \end{aligned} \tag{B2}$$

where J_1 is a first-order Bessel function of the first kind and $r = \sqrt{x^2+y^2}$ is the separation distance of the two points. The second relation relies on a polar coordinate transform and an assumption of isotropic flow statistics, that is, $\nabla\cdot\mathrm{SF}_{uuu} = r^{-1}\partial_r(r\mathrm{SF}_{Luu})$. It can be seen in Figs. B1–B3 that in anisotropic flows, structure functions are also anisotropic and third-order structure functions are typically more anisotropic than advective structure functions, consistent with the 2D turbulence results of Pearson et al. (2021).

In two-dimensional systems, this can be integrated by parts to create an integral of the structure function, rather than its (noisier) derivative (Xie and Bühler 2018),

$$\begin{aligned} \Pi_K^u &= -\frac{K}{4}\int\frac{\partial(r\mathrm{SF}_{Luu})}{\partial r}\left[\frac{1}{r}J_1(Kr)\right]dr \\ &= -\frac{K}{4}\int_0^{\infty}\mathrm{SF}_{Luu}KJ_2(Kr)dr - \frac{K}{4}[\mathrm{SF}_{Luu}J_1(Kr)]_0^{\infty} \\ &\approx -\frac{K^2}{4}\int_0^{\infty}\mathrm{SF}_{Luu}J_2(Kr)dr, \end{aligned} \tag{B3}$$

where we have utilized the property that $\partial_x(x^{-n}J_n) = -xJ_{n+1}$. Note that the final result is only true if the first term of the second line converges to zero as $r \to \infty$, which requires SF_{Luu} has a slope shallower than $r^{1/2}$ at the largest scales.

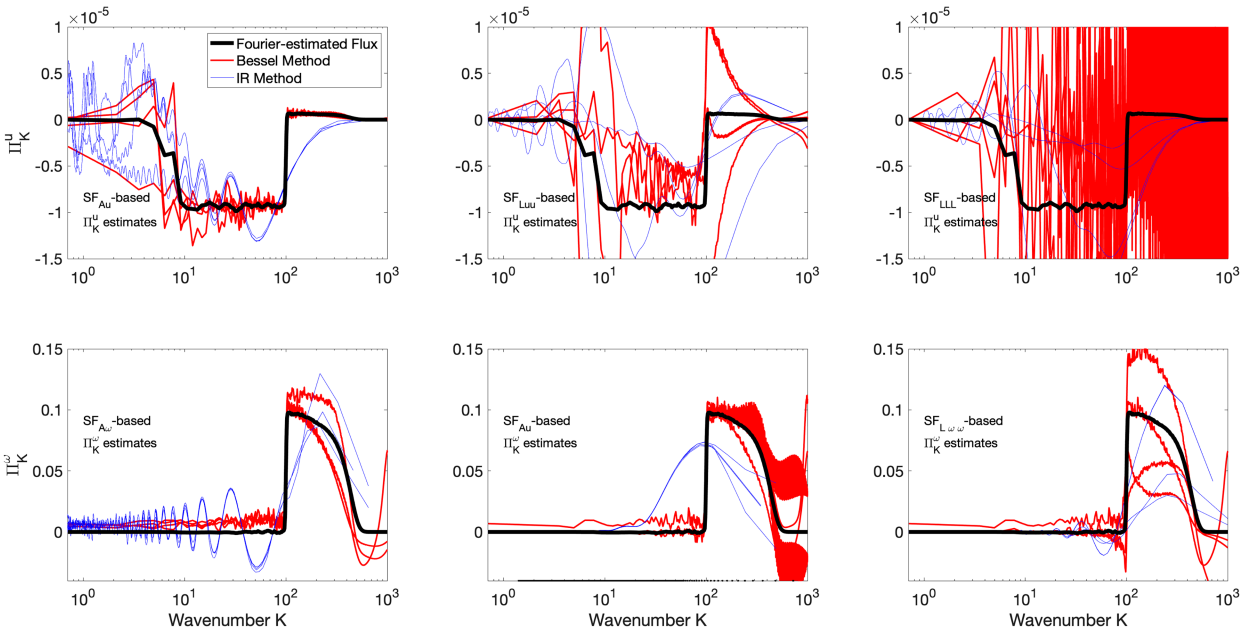

FIG. B1. Spectral energy flux Π^u_K and enstrophy flux Π^ω_K estimates in simulated anisotropic 2D turbulence from advective and third-order SFs. Shown are the diagnosed fluxes (black lines) and flux estimates from SFs via the new Bessel transform method (red lines) and IR methods (blue lines). Energy flux estimates are shown using the (top left) advective velocity SF, (top center) third-order velocity SF, and (top right) third-order longitudinal SF. Enstrophy flux estimates are shown using (bottom left) the advective vorticity SF, (bottom center) the advective velocity SF, and (bottom right) $\mathrm{SF}_{L\omega\omega}$. Flux estimates show four lines, each representing a different orientation for the SF separation vector (across- and along-isotropy axis and two diagonals; as shown in Fig. 2). For IR methods, we map $\mathrm{SF}(r) \rightarrow \Pi(K)$ using $K = \beta/r$, where $\beta = (2, 3.1, 4.3, 2, 1.5, 3.1)$ for the respective panels following Bessel function arguments (see text).

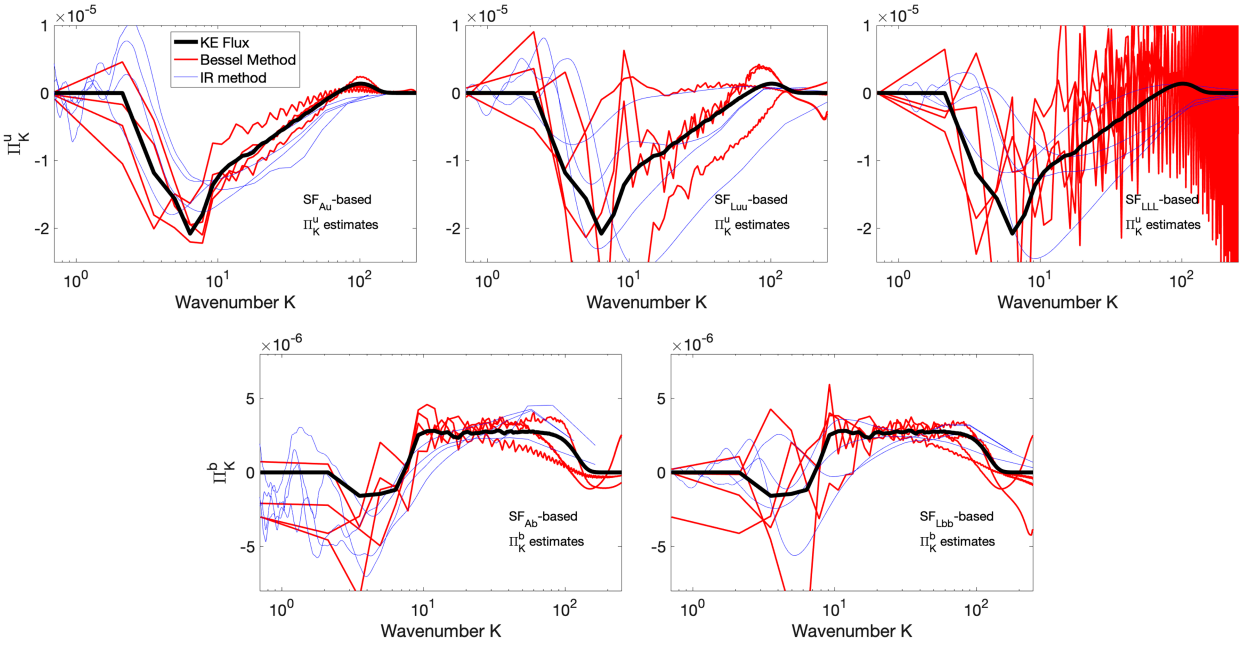

FIG. B2. Spectral KE flux Π^u_K and buoyancy variance flux Π^b_K estimates in simulated anisotropic SQG turbulence from advective and third-order SFs. KE flux estimates are shown using (top left) advective velocity SF, (top center) third-order velocity SF, and (top right) third-order longitudinal SF. Buoyancy variance flux estimates are shown using the (bottom left) advective buoyancy SF and (bottom right) third-order longitudinal buoyancy SF. IR methods are mapped using $\beta = (2, 3.1, 4.3, 2, 3.1)$, respectively. See Fig. B1 for line descriptions.

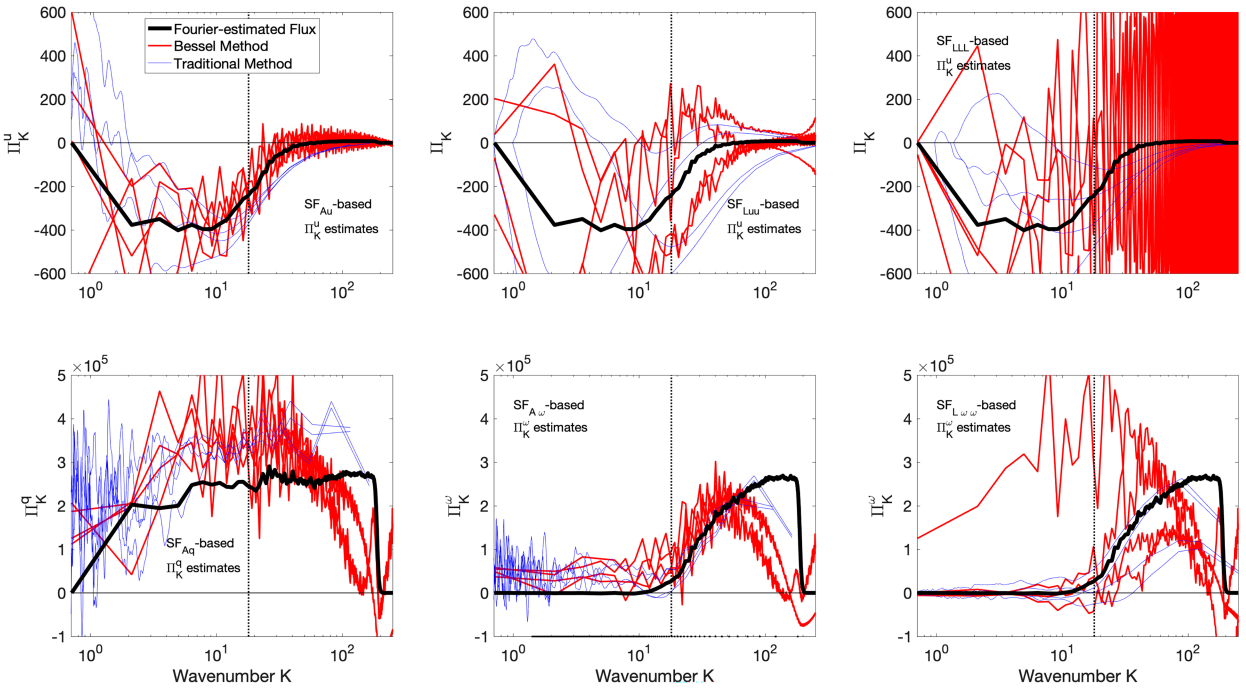

FIG. B3. Estimates of top-layer spectral fluxes in simulated anisotropic two-layer QG turbulence from advective and third-order SFs. Panels show estimates of the (top) energy flux Π^u_K, (bottom left) potential enstrophy flux Π^q_K, and (bottom center),(bottom right) enstrophy Π^ω_K. Estimates are made using the (top left) advective velocity SF, (top center) third-order total velocity SF, (top right) third-order longitudinal velocity SF, (bottom left) advective potential vorticity SF, (bottom center) advective vorticity SF, and (bottom right) third-order vorticity SF. IR methods are mapped using $\beta = (2, 3.1, 4.3, 2, 2, 3.1)$, respectively. See Fig. B1 for line descriptions.

This can also be reframed in terms of SF_{LLL} by using the relation $\mathrm{SF}_{Luu} = (1/3r^2)[\partial(r^3\mathrm{SF}_{LLL})/\partial r]$ (Xie and Bühler 2018). Then,

$$\Pi^u_K = -\frac{K^3}{12}\int_0^\infty \mathrm{SF}_{LLL}J_3(Kr)rdr - \frac{K^2}{12}[r\mathrm{SF}_{LLL}J_2(Kr) + 3\mathrm{SF}_{Luu}J_1(Kr)]_0^\infty. \tag{B4}$$

These SF_{Luu} and SF_{LLL} methods for estimating spectral kinetic energy fluxes have significant noise and directional variability in a 2D system (Fig. B1) in an SQG system (Fig. B2) and in a two-layer QG system (Fig. B3).

More generally, an equivalent relation to Eq. (B2) can be derived by noting the interchangeability of advective and third-order structure functions in incompressible flow $\mathrm{SF}_{\mathcal{A}u} = \delta\mathcal{A}_u \cdot \delta\mathbf{u} = (1/2)\nabla\cdot|\delta\mathbf{u}|^2\delta\mathbf{u}$:

$$\Pi^u_K = -\frac{1}{2}\iint \widetilde{(\mathrm{SF}_{\mathcal{A}u})}H(K-\kappa)dkdl = -\frac{1}{4\pi}\iint \mathrm{SF}_{\mathcal{A}u}\frac{K}{r}J_1(Kr)dxdy$$
$$= -\frac{K}{2}\int \widetilde{\mathrm{SF}}_{\mathcal{A}u}J_1(Kr)dr. \tag{B5}$$

For any advected scalar (nominally vorticity ω), and the spectral flux of its halved variance (nominally Π^ω_K, the flux of enstrophy $\eta = \omega^2/2$), we can follow steps analogous to the above energy derivation to arrive at a set of relations between Π^ω_K and both the vorticity and velocity advective structure functions [noting that $\mathrm{SF}_{\mathcal{A}\omega} = \nabla^2(\mathrm{SF}_{\mathcal{A}u})$]:

$$\Pi^\omega_K = -\frac{K}{2}\int_0^\infty \widetilde{\mathrm{SF}}_{\mathcal{A}\omega}J_1(Kr)dr$$
$$= \frac{K}{2}\int_0^\infty \nabla_r^2(\widetilde{\mathrm{SF}}_{\mathcal{A}u})J_1(Kr)dr.$$
$$= \frac{K}{2}\int_0^\infty \frac{1}{r}\frac{\partial}{\partial r}\left(\frac{1}{r}\frac{\partial\widetilde{\mathrm{SF}}_{\mathcal{A}u}}{\partial r}\right)J_1(Kr)dr. \tag{B6}$$

Evaluating this relationship leads to the following relationship for the advective velocity structure function:

$$\Pi^\omega_K = \frac{K^3}{2}\int_0^\infty \widetilde{\mathrm{SF}}_{\mathcal{A}u}\left[J_3(Kr) - \frac{2}{Kr}J_2(Kr)\right]dr$$
$$+ \frac{K^2}{2}\left[\widetilde{\mathrm{SF}}_{\mathcal{A}u}J_2(Kr) + K\frac{d\widetilde{\mathrm{SF}}_{\mathcal{A}u}}{dr}J_1(Kr)\right]_{r=0}^\infty. \tag{B7}$$

Under the assumption that $\mathrm{SF}_{\mathcal{A}u} \to 0$ at small scales and has no slope at large scales, the nonintegral part of this relation disappears. This would allow the diagnosis of the enstrophy flux via

$$\Pi^\omega_K = \frac{K^3}{2}\int_0^\infty \widetilde{\mathrm{SF}}_{\mathcal{A}u}\left[J_3(Kr) - \frac{2}{Kr}J_2(Kr)\right]dr$$
$$= \frac{K^3}{2}\int_0^\infty \widetilde{\mathrm{SF}}_{\mathcal{A}u}\left[\frac{2}{Kr}J_2(Kr) - J_1(Kr)\right]dr, \tag{B8}$$

where we have utilized Bessel function properties to write expressions in terms of different-order Bessel functions. Furthermore, it follows from Eq. (17) that

$$\Pi_K^{\omega} = -\frac{K^2}{4}\int_0^{\infty} \widetilde{SF}_{L\omega\omega} J_2(Kr)dr - \frac{K}{4}[\widetilde{SF}_{L\omega\omega} J_1(Kr)]_0^{\infty}. \quad \text{(B9)}$$

This $\mathrm{SF}_{L\omega\omega} = \overline{\delta u_L \delta\omega\delta\omega}$ method for estimating spectral enstrophy fluxes has significant directional variability in 2D turbulence (Fig. B1) and QG turbulence (Fig. B3), while the analogous SF_{Lbb} method for estimating the spectral flux of buoyancy variance produces reasonable estimates in SQG turbulence (Fig. B2).

REFERENCES

Abramowitz, M., and I. A. Stegun, 1948: *Handbook of Mathematical Functions with Formulas, Graphs, and Mathematical Tables.* National Bureau of Standards Applied Mathematics Series, Vol. 55, U.S. Government Printing Office, 470 pp., https://personal.math.ubc.ca/~cbm/aands/abramowitz_and_stegun.pdf.

Aluie, H., 2019: Convolutions on the sphere: Commutation with differential operators. *GEM-Int. J. Geomath.*, **10**, 9.

——, M. Hecht, and G. K. Vallis, 2018: Mapping the energy cascade in the North Atlantic Ocean: The coarse-graining approach. *J. Phys. Oceanogr.*, **48**, 225–244, https://doi.org/10.1175/JPO-D-17-0100.1.

Arbic, B. K., R. B. Scott, G. R. Flierl, A. J. Morten, J. G. Richman, and J. F. Shriver, 2012: Nonlinear cascades of surface oceanic geostrophic kinetic energy in the frequency domain. *J. Phys. Oceanogr.*, **42**, 1577–1600, https://doi.org/10.1175/JPO-D-11-0151.1.

Balwada, D., J.-H. Xie, R. Marino, and F. Feraco, 2022: Direct observational evidence of an oceanic dual kinetic energy cascade and its seasonality. *Sci. Adv.*, **8**, eabq2566, https://doi.org/10.1126/sciadv.abq2566.

Boffetta, G., and R. E. Ecke, 2012: Two-dimensional turbulence. *Annu. Rev. Fluid Mech.*, **44**, 427–451, https://doi.org/10.1146/annurev-fluid-120710-101240.

Capet, X., P. Klein, B. L. Hua, G. Lapeyre, and J. C. Mcwilliams, 2008: Surface kinetic energy transfer in surface quasi-geostrophic flows. *J. Fluid Mech.*, **604**, 165–174, https://doi.org/10.1017/S0022112008001110.

Chelton, D. B., M. G. Schlax, and R. M. Samelson, 2011: Global observations of nonlinear mesoscale eddies. *Prog. Oceanogr.*, **91**, 167–216, https://doi.org/10.1016/j.pocean.2011.01.002.

Constantinou, N. C., G. L. Wagner, L. Siegelman, B. C. Pearson, and A. Palóczy, 2021: GeophysicalFlows.jl: Solvers for geophysical fluid dynamics problems in periodic domains on CPUs GPUs. *J. Open Source Software*, **6**, 3053, https://doi.org/10.21105/joss.03053.

Contreras, M., L. Renault, and P. Marchesiello, 2023: Understanding energy pathways in the Gulf Stream. *J. Phys. Oceanogr.*, **53**, 719–736, https://doi.org/10.1175/JPO-D-22-0146.1.

Davidson, P. A., 2004: *Turbulence: An Introduction for Scientists and Engineers.* Oxford University Press, 657 pp.

Delpech, A., R. Barkan, K. Srinivasan, J. C. McWilliams, B. K. Arbic, O. Q. Siyanbola, and M. C. Buijsman, 2024: Eddy–internal wave interactions and their contribution to cross-scale energy fluxes: A case study in the California Current. *J. Phys. Oceanogr.*, **54**, 741–754, https://doi.org/10.1175/JPO-D-23-0181.1.

Deusebio, E., P. Augier, and E. Lindborg, 2014: Third-order structure functions in rotating and stratified turbulence: A comparison between numerical, analytical and observational results. *J. Fluid Mech.*, **755**, 294–313, https://doi.org/10.1017/jfm.2014.414.

Frisch, U., 1995: *Turbulence.* Cambridge University Press, 296 pp.

Garabato, A. C. N., X. Yu, J. Callies, R. Barkan, K. L. Polzin, E. E. Frajka-Williams, C. E. Buckingham, and S. M. Griffies, 2022: Kinetic energy transfers between mesoscale and submesoscale motions in the open ocean's upper layers. *J. Phys. Oceanogr.*, **52**, 75–97, https://doi.org/10.1175/JPO-D-21-0099.1.

Hewitt, H., B. Fox-Kemper, B. Pearson, M. Roberts, and D. Klocke, 2022: The small scales of the ocean may hold the key to surprises. *Nat. Climate Change*, **12**, 496–499, https://doi.org/10.1038/s41558-022-01386-6.

Johnson, G. C., and Coauthors, 2022: Argo—Two decades: Global oceanography, revolutionized. *Annu. Rev. Mar. Sci.*, **14**, 379–403, https://doi.org/10.1146/annurev-marine-022521-102008.

Klein, P., and Coauthors, 2019: Ocean-scale interactions from space. *Earth Space Sci.*, **6**, 795–817, https://doi.org/10.1029/2018EA000492.

Kolmogorov, A. N., 1941: The local structure of turbulence in incompressible viscous fluid for very large Reynolds numbers. *Dokl. Akad. Nauk SSSR*, **30**, 299–303.

Kraichnan, R. H., 1967: Inertial ranges in two-dimensional turbulence. *Phys. Fluids*, **10**, 1417–1423, https://doi.org/10.1063/1.1762301.

Lapeyre, G., 2017: Surface quasi-geostrophy. *Fluids*, **2**, 7, https://doi.org/10.3390/fluids2010007.

Lindborg, E., 1996: A note on Kolmogorov's third-order structure-function law, the local isotropy hypothesis and the pressure–velocity correlation. *J. Fluid Mech.*, **326**, 343–356, https://doi.org/10.1017/S0022112096008348.

——, 1999: Can the atmospheric kinetic energy spectrum be explained by two-dimensional turbulence? *J. Fluid Mech.*, **388**, 259–288, https://doi.org/10.1017/S0022112099004851.

McCaffrey, K., B. Fox-Kemper, and G. Forget, 2015: Estimates of ocean macroturbulence: Structure function and spectral slope from Argo profiling floats. *J. Phys. Oceanogr.*, **45**, 1773–1793, https://doi.org/10.1175/JPO-D-14-0023.1.

Morrow, R., L.-L. Fu, M.-H. Rio, R. Ray, P. Prandi, P.-Y. L. Traon, and J. Benveniste, 2023: Ocean circulation from space. *Surv. Geophys.*, **44**, 1243–1286, https://doi.org/10.1175/JPO-D-14-0023.1.

Nie, Q, and S. Tanveer, 1999: A note on third–order structure functions in turbulence. *Proc. Roy. Soc.*, **455A**, 1615–1635, https://doi.org/10.1098/rspa.1999.0374.

Pearson, B., 2025: BrodiePearson/paper_Bessel_SF_Method: Submitted_version. Zenodo, https://doi.org/10.5281/zenodo.14868825.

Pearson, B. C., J. L. Pearson, and B. Fox-Kemper, 2021: Advective structure functions in anisotropic two-dimensional turbulence. *J. Fluid Mech.*, **916**, A49, https://doi.org/10.1017/jfm.2021.247.

Pearson, J., and Coauthors, 2020: Biases in structure functions from observations of submesoscale flows. *J. Geophys. Res. Oceans*, **125**, e2019JC015769, https://doi.org/10.1029/2019JC015769.

Rivera, M., H. Aluie, and R. E. Ecke, 2014: The direct enstrophy cascade of two-dimensional soap film flows. *Phys. Fluids*, **26**, 055105, https://doi.org/10.1063/1.4873579.

Salmon, R., 1980: Baroclinic instability and geostrophic turbulence. *Geophys. Astrophys. Fluid Dyn.*, **15**, 167–211, https://doi.org/10.1080/03091928008241178.

Silvestri, S., and Coauthors, 2025: A GPU-based ocean dynamical core for routine mesoscale-resolving climate simulations. *J.*

Adv. Model. Earth Syst., **17**, e2024MS004465, https://doi.org/10.1029/2024MS004465.

Smith, K. S., and G. K. Vallis, 2002: The scales and equilibration of midocean eddies: Forced–dissipative flow. *J. Phys. Oceanogr.*, **32**, 1699–1720, https://doi.org/10.1175/1520-0485(2002)032<1699:TSAEOM>2.0.CO;2.

——, G. Boccaletti, C. C. Henning, I. Marinov, C. Y. Tam, I. M. Held, and G. K. Vallis, 2002: Turbulent diffusion in the geostrophic inverse cascade. *J. Fluid Mech.*, **469**, 13–48, https://doi.org/10.1017/S0022112002001763.

Storer, B. A., and H. Aluie, 2023: FlowSieve: A coarse-graining utility for geophysical flows on the sphere. *J. Open Source Software*, **8**, 4277, https://doi.org/10.21105/joss.04277.

——, M. Buzzicotti, H. Khatri, S. M. Griffies, and H. Aluie, 2022: Global energy spectrum of the general oceanic circulation. *Nat. Commun.*, **13**, 5314, https://doi.org/10.1038/s41467-022-33031-3.

Vallis, G. K., 2006: *Atmospheric and Oceanic Fluid Dynamics: Fundamentals and Large-Scale Circulation.* Cambridge University Press, 745 pp.

Wagner, C., B. Pearson, and A. Lee, 2024: FluidSF. Zenodo, https://doi.org/10.5281/zenodo.11406185.

Webb, E. K., 1964: Ratio of spectrum and structure-function constants in the inertial subrange. *Quart. J. Roy. Meteor. Soc.*, **90**, 344–346, https://doi.org/10.1002/qj.49709038520.

Xie, J.-H., and O. Bühler, 2018: Exact third-order structure functions for two-dimensional turbulence. *J. Fluid Mech.*, **851**, 672–686, https://doi.org/10.1017/jfm.2018.528.

——, and ——, 2019: Third-order structure functions for isotropic turbulence with bidirectional energy transfer. *J. Fluid Mech.*, **877**, R3, https://doi.org/10.1017/jfm.2019.651.

Zhang, D., J. Song, Y. Gao, Y. Peng, J. Hu, F. G. Schmitt, and Y. Huang, 2024: Scale-to-scale energy flux in the oceanic global circulation models. *Front. Mar. Sci.*, **11**, 1307751, https://doi.org/10.3389/fmars.2024.1307751.